$BaTiO_3$ based materials for Piezoelectric and Electro-Optic Applications

by

Ytshak Avrahami

B.Sc. Materials Science and Engineering, B.A. Physics (Cum Laude)

Technion – Israel Institute of Technology, 1995

M.Sc. Materials Science and Engineering

Technion – Israel Institute of Technology, 1997

SUBMITTED TO THE DEPARTMENT OF MATERIALS SCIENCE AND ENGINEERING IN PARTIAL FULFILLMENT OF THE REQUIREMENTS FOR THE DEGREE OF

DOCTOR OF PHILOSOPHY IN ELECTRONIC, PHOTONIC AND MAGNETIC MATERIALS

JANUARY 2003

$BaTiO_3$ based materials for Piezoelectric and Electro-Optic Applications

by

Ytshak Avrahami

Submitted to the Department of Materials Science and Engineering on February 13, 2003 in Partial Fulfillment of the Requirements for the Degree of Doctor OF Philosophy in Electronic, Photonic and Magnetic Materials

ABSTRACT

Ferroelectric materials are key to many modern technologies, in particular piezoelectric actuators and electro-optic modulators. $BaTiO_3$ is one of the most extensively studied ferroelectric materials. The use of $BaTiO_3$ for piezoelectric applications is, however, limited due to the small piezoelectric coefficient of the room temperature-stable tetragonal phase. Furthermore, research on $BaTiO_3$ for integrated optics applications remains sparse.

In this work Zr-, Hf-, and KNb- doped $BaTiO_3$ materials were prepared in a composition range that stabilizes the rhombohedral phase. These materials were prepared as bulk polycrystals using a standard solid-state reaction technique in order to test the piezoelectric and dielectric properties. Some compositions were then chosen for thin film deposition. The films were deposited using pulsed laser deposition on MgO and SOI substrates. Growth orientation, remnant strain and optical properties were then measured.

X-ray diffraction was used to confirm the existence of a stable rhombohedral phase. Dielectric measurements confirmed the expected phase transition temperatures. A piezoelectric coefficient of d_{33}=290-470pc/N was measured for Zr- and Hf- doped $BaTiO_3$, compared with d_{33}=75pC/N for pure $BaTiO_3$. The electrostrictive coefficient of the KNb-doped material, was measured as $Q_{33}=0.37m^4/C^2$, compared with $Q_{33}=0.11m^4/C^2$ for pure $BaTiO_3$. The maximum strain measured for the doped samples was 5-10 times higher then that of pure $BaTiO_3$.

The effect of growth conditions on the orientation and strain of $BaTiO_3$ thin films was studied. As the substrate temperature and laser fluency were increased the film orientation varied from (111) to (110), then to (100). Zr- and Hf- doping helped lower the forming temperature for the different orientations.

The index of refraction for the thin films was measured and a model based on the Clausius-Mossotti relation was used to explain the data. The refractive index for $BaTiO_3$ films was extracted from the model, giving n_o=2.334 and n_e=2.163.

Thesis Supervisor: Harry L. Tuller

Title: Professor of Ceramics and Electronic Materials

Biographical Note

Education

Department of Materials Science and Engineering, MIT, Cambridge, MA, USA.

2003 – Ph.D. Electronic, Optical and Magnetic Materials. Thesis topic:

'BaTiO3 based materials for piezoelectric and electro-optic applications'.

Department of Materials Engineering, Technion-Israel Institute of Technology, Haifa, Israel.

1995 - B.Sc., Materials Engineering and B.A, Physics (Cum Laude).

1997 - M.Sc. in Materials Engineering. Thesis topic:

'Characterization of Waveguide Fabrication Processes in LiNbO3'.

Awards

The Shenkar scholarship for research in materials engineering. (May 1997).

The Miriam and Aharon Gutwirt scholarship of excellence. (March 1997).

E-MRS Young Scientist Award. E-MRS 96 Spring meeting, Strasbourg, France (1996).

Materials Engineering Dean's Award for excellence in studies. (1995 academic year).

Technion President's Award for excellence in studies. (1994 academic year).

Publications

1. Zolotoyabko, E. and Avrahami, Y., "*Characterization of Optical Wave-Guide Layers in $LiNbO_3$ by High-Resolution X-ray Diffraction*", Mater. Lett. 24 (4), *p.* 215-9(1995).
2. Avrahami, Y. and Zolotoyabko, E., "*Structural modifications in He-implanted waveguide layers of $LiNbO_3$*", Nucl. Inst. Meth. B 120 (1-4), *p.* 84-7(1996).
3. Zolotoyabko, E., Avrahami, Y., Sauer, W., Metzger, T.H. and Peisl, J., "*Strain profiles in He-implanted waveguide layers of $LiNbO_3$ crystals*", Mater. Lett. 27 (1-2), *p.* 17-20(1996).
4. Sauer, W., Metzger, T.H., Peisl, J., Avrahami, Y. and Zolotoyabko, E., "*Grazing-incidence diffraction on LiNbO3 under surface acoustic wave excitation*", Nuovo Cimento Della Societa Italiana Di Fisica D-condensed Matter Atomic Molecular and Chemical Physics Fluids Plasmas Biophysics 19 (2-4), *p.* 455-63(1997).
5. Zolotoyabko, E., Avrahami, Y., Sauer, W., Metzger, T.H. and Peisl, J., "*High-temperature phase transformation in Ti-diffused waveguide layers of $LiNbO_3$*", Appl. Phys. Lett. 73 (10), *p.* 1352-4(1998).
6. Sauer, W., Metzger, T.H., Peisl, J., Avrahami, Y. and Zolotoyabko, E., "*X-ray diffraction under surface acoustic wave excitation*", Physica B 248, *p.* 358-65(1998).
7. Avrahami, Y., Shilo, D., Mainzer, N. and Zolotoyabko, E., "*Study of atomic diffusion in crystalline structures by high-resolution X-ray diffraction*", J. Cryst. Growth 199, *p.* 264-9(1999).
8. Avrahami, Y. and Zolotoyabko, E., "*Diffusion and structural modification of Ti : $LiNbO_3$, studied by high-resolution x-ray diffraction*", J. Appl. Phys. 85 (9), *p.* 6447-52(1999).
9. Avrahami, Y., Zolotoyabko, E., Sauer, W., Metzger, T.H. and Peisl, J., "*Structure of the near-surface waveguide layers produced by diffusion of titanium in lithium niobate*", Materials Research Society Symposium Proceedings, Vol. 590, Boston, 2000 p. 213-218.
10. Tuller, H. and vrahami, Y., "*Stabilized Barium Titanate Thin Film Structures*", App. Num. 60/405,297, Pat. Pending, 2002 .
11. Tuller, H.L. and Avrahami, Y. *Electroceramics*. in "Encyclopedia of Smart Materials"; edited by Schwartz, M.M. (John Wiley & Sons, New York, 2002) .
12. Avrahami, Y. and Tuller, H., "*Rhombohedral-phase doped barium titanate as a piezoelectric transducer*", App. Num. US06744 200103, Pat. Pending, 2002.

Acknowledgments

As with every work of science, there are many people who have helped. First I would like to thank the agencies that funded my research. The research started under a grant from the ARO (DAAH04-95-1-0104) to a lab that no longer exists (AMSL), it continued with support from a company since gone (Nanovation), and finally found a place with Pirelli corp. under the MIT-Pirelli alliance. I would like to thank the people at Pirelli, especially Daniele, Luciano and Paola, for the valuable input and the assistance with some of the optical measurements.

No thesis can be achieved without the help of an advisor. I would like to thank Prof. Harry Tuller for steering me in the right direction when side projects became too demanding, and for helping me make the most out of my stay at MIT.

To the other members of the group, for all the distractions that they offered – from coffee breaks, to ski trips. I would especially like to thank Todd for all his help in processing and purchasing.

Life is not just work, and there are many people who deserve thanks outside of MIT. I'd like to thank my wife, Keren, for being patient each time the degree seemed to stretch an extra month (and for catching all the missing verbs in this thesis). Let's not forget my parents, Edi and Eli, and my sisters Michal and Yael – who never passed the opportunity to make fun of me each time the degree seemed to stretch an extra month.

Table of Contents

List of figures

List of Tables

Chapter 1: Background

1. Introduction

Ferroelectric materials are key to many modern technologies. Computers use ferroelectric memories, security systems use pyroelectric sensors, cell phones need better dielectrics to improve antenna reception, optical communication components require electro-optic films and piezoelectric transducers are used for many purposes, ranging from micro-speakers to medical ultrasound. Traditional materials design looks at measurable quantities, such as dielectric constant, or piezoelectric coefficient. Recently, however, the issue of environmental impact is becoming more important as a design parameter. This has spurred a search for alternative ferroelectrics to the many lead-based systems currently in use.

$BaTiO_3$ is a commonly used ferroelectric as a high permittivity dielectric, as a PTC (positive thermal coefficient) material, and as a pyroelectric sensor. In this work, $BaTiO_3$-based materials are considered for a wider range of applications, namely lead-free piezoelectric actuators and electro-optic modulators. The two seemingly separate applications are a result of the transition from a project funded by the ARO on actuator materials to industry funded research under the Microphotonics center. There are, however, many issues in common for both applications. In particular, one can consider an integrated optics circuit with $BaTiO_3$-based materials serving both as electro-optic materials and as actuator materials for MEMS based devices. Furthermore, the piezoelectric and dielectric responses are very important when designing electro-optic devices.

With the actuator and electro-optic modulator applications in mind, the following sections will generally be divided into two major parts – bulk materials analysis, focusing on the piezoelectric properties, and thin film analysis, focusing on the optical properties.

2. Piezoelectric Actuators

2.1. General

Piezoelectric materials are materials that undergo a mechanical strain and electrical polarization due to an applied electric field. The first listing of piezoelectric materials was collected by Victor Moritz Goldschmidt in 1926 [1]. It was not until the 1940's that barium titanate was discovered to be a ferroelectric exhibiting an exceptionally high dielectric constant [2].

Polarization requires a non-symmetric structure; therefore all crystallographic point groups that have a center of symmetry can not show piezoelectricity. Furthermore, the cubic class 432, although lacking a center of symmetry, can not accommodate piezoelectricity. We are, therefore, left with 20 of the 32 crystallographic point groups that show piezoelectricity. Of these groups, 10 have a unique crystallographic axis and therefore can have an electric dipole even at zero applied field (electric and mechanical). These materials are defined as pyroelectric and show a change of polarization due to a change in temperature [3].

Pyroelectric materials include a sub-class of material in which an applied external field can change the direction of polarization. These materials are referred to as ferroelectric. In some cases, although a polar unit cell exists in the material, the overall behavior is non polar. Materials that have polar sub-cells organized such that adjacent sub-cells have opposite polarization are called anti-ferroelectric. The relationship between the different symmetry groups and the polarization properties are shown in Figure 1.

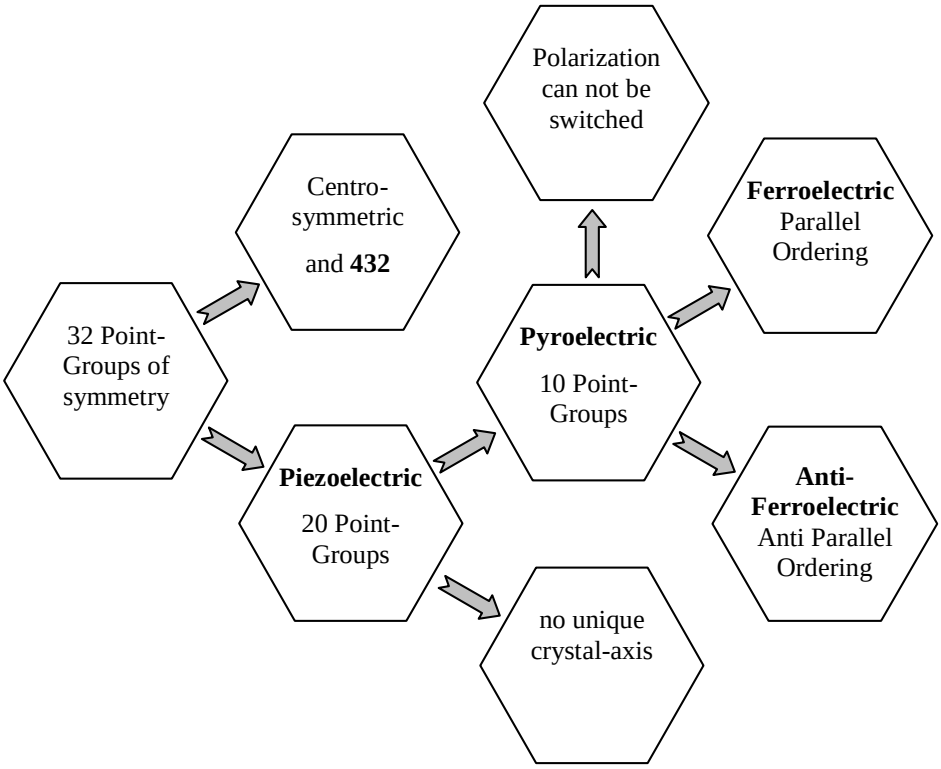

Figure 1: Crystallographic symmetry groups and polarized materials.

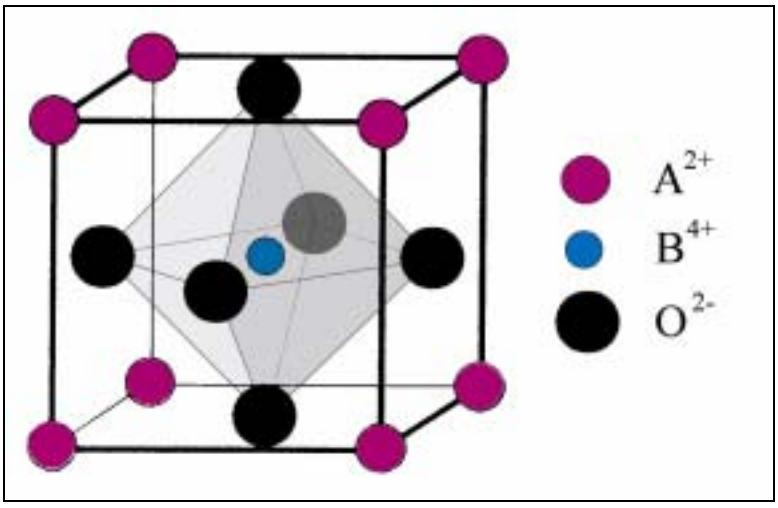

Figure 2: Cubic perovskite unit cell showing the oxygen octahedra and the ionic positions for the A and B cations.

Many materials used for electromechanical actuation have the basic perovskite structure $A^{II}B^{IV}O_3$. The unit cell of the high temperature cubic structure is shown in Figure 2. Lowering the temperature results in a reduction of symmetry and the structure transforms into either the tetragonal, rhombohedral or orthorhombic phase. The ferroic phase transition occurs due to a long-range interaction between atomic dipoles. Such interactions can be described quantitatively on two scale levels, macroscopic parameters and microscopic interactions.

2.2. Important Piezoelectric Parameters

The piezoelectric modulus *d* is a third rank tensor that relates the polarization (P_i) to the applied stress, σ_{jk}:

$$P_i = d_{ijk}\sigma_{jk} \tag{1}$$

The converse piezoelectric effect relates changes in crystal shape and size to an applied electric field. It can be shown that the coefficient relating strain (ε_{ij}) to the applied electric field (E_k) is identical to the direct piezoelectric modulus in a way that we can write:

$$\varepsilon_{jk} = d_{ijk}E_i \tag{2}$$

or in terms of the Polarization:

$$\varepsilon_{jk} = b_{ijk}P_i \tag{3}$$

For a detailed discussion about the tensor behavior of the piezoelectric coefficient and a proof of the equality of the direct and converse effects see Nye [4] chapters VII and X.

The piezoelectric coefficient is a very important parameter for piezoelectric actuators. There are, however, other important parameters to consider in such materials.

The polarization is not an easy property to measure. In many sensors, the measured variable is the voltage, or the electric field (E), that is induced due to an applied stress

(σ). The relationship between the field and the stress is given by the piezoelectric voltage constant g:

$$E_i = g_{ijk}\sigma_{jk} \tag{4}$$

Taking into account the relationship between the electric field and polarization, one can readily show that the two piezoelectric constants are related by:

$$g = d/\varepsilon \cdot \varepsilon_0 \tag{5}$$

The above is a simplified form of the tensor relations, which holds for either homogeneous materials or along principal axes.

Both the strain and the voltage piezoelectric constants give the magnitude of the effect, however they do not tell us how efficient the system will be in converting electrical to mechanical energy and vice versa. There are three parameters that describe the transfer between electrical and mechanical energies:

1. Efficiency: η=(output energy) / (consumed energy)

2. Energy transmission coefficient: λ_{max}= [(output energy) / (input energy)]$_{max}$

3. Electromechanical coupling factor: k^2=(stored energy) / (input energy)

Although the differences between these parameters are small, they are important. They are not, however, independent. It can be shown that the electromechanical coupling coefficient is related to the stiffness (c) or the compliance (s), and to the piezoelectric and dielectric constants by [5]:

$$k^2 = d^2 c/\varepsilon \cdot \varepsilon_0 = d^2/s \cdot \varepsilon \cdot \varepsilon_0 \tag{6}$$

From this, the relationship between the coupling coefficient and the energy transmission coefficient can be calculated as:

$$\lambda_{\max} = \left[\left(1/k\right) - \sqrt{\left(1/k^2\right) - 1}\right]^2 \tag{7}$$

By taking the consumed energy to be the difference between input and output energies, the relationship between the efficiency and the energy transmission can be written as:

$$\eta = \frac{\lambda_{\max}}{1-\lambda_{\max}} \tag{8}$$

Piezoelectric materials have a characteristic electromechanical resonance frequency. Close to that frequency, the material response is highly non-linear and the parameters described above are insufficient. The resonance behavior is very important for applications such as sensors and ultrasonic motors. To describe the quality of the resonance (Q) in the material around the resonance frequency (ω_0), the frequency width ($\Delta\omega$) of the resonance is used:

$$Q_m = \varpi_0 / 2\Delta\varpi \tag{9}$$

A full description of resonators and acoustic wave sensors is beyond the scope of this thesis. A comprehensive coverage of the topic can be found in reference [6].

Table 1 summarizes these figures of merit, and gives typical units for them.

Table 1: Figures of merit for piezoelectric materials[3]. Symbol definitions can be found in the text.

Figure of merit	Parameter [units]	Important relations
Piezoelectric strain constant	$d\left[C/N\right]$	$\varepsilon_{jk} = d_{ijk}E_i \ , \ P_i = d_{ijk}\sigma_{jk}$
Piezoelectric voltage constant	$g\left[V \cdot m/N\right]$	$E_i = g_{ijk}\sigma_{jk} \ , \ g = d/\varepsilon \cdot \varepsilon_0$
Electromechanical coupling coefficient	k^2 [--]	$k^2 = d^2 c/\varepsilon \cdot \varepsilon_0 = d^2/s \cdot \varepsilon \cdot \varepsilon_0$
Mechanical quality factor	Q_m [--]	$Q_m = \omega_0/2\Delta$

2.3. Electrostrictive Materials

Electrostriction is the second order piezoelectric response, correlating strain (ε) with electric field (E) [7]:

$$\varepsilon_{ij} = M_{ijkl}E_kE_l$$

This is a second order effect, and therefore it is not limited to any particular crystal symmetry. Although all materials show some level of electrostriction, the effect is often times small. For most piezoelectric materials the strain due to electrostriction is much smaller then the strain due to piezoelectricity, making it undetectable. In some cases, however, electrostriction can actually result in strains comparable to PZT piezoelectrics. One example for such a material system is $Pb(Mg_{1/3}Mn_{2/3})O_3$, a relaxor ferroelectric[8].

Electrostriction can be written with respect to polarization (P), rather then electric field:

$$\varepsilon_{ij} = Q_{ijkl}P_kP_l \qquad (10)$$

The polarization is related to the electric field through the dielectric constant [9]:

$$P = P_s + \varepsilon \cdot \varepsilon_0 E \qquad (11)$$

This leads to the relationship between the two coefficients:

$$M = (\varepsilon\varepsilon_0)^2 Q \qquad (12)$$

3. Materials Used for Electromechanical Actuation

3.1. PZT as an Active Material

The most commonly used electromechanically active perovskites are lead - zirconate - titanate (PZT) based. These materials have a composition of $Pb(Zr_xTi_{1-x})O_3$ with $x \approx 0.5$ near the morphotropic phase boundary. The use of these materials is limited to relatively small displacements as the highest strain level achieved is $\varepsilon_{max} \approx 0.15\%$ [10]. Another limitation of PZT based materials is the fact that they are lead-based. Lead has a high vapour pressure at elevated temperatures, making the manufacturing process more complicated and environmentally hazardous.

3.2. FE-AFE Phase Transition Actuation

In order to increase strain levels, a field induced ferroelectric (FE) - antiferroelectric (AFE) phase transition may be used. PZT based materials, near the morphotropic phase boundary at $x \approx 0.05$ are used. Previous research in our group [11] showed that for PLZHT ($Pb_{1-x}La_x(Zr_{1-y}Hf_y)_{1-z}Ti_zO_3$) the strain accompanying the phase transition can be as high as 0.4%.

Figure 4a shows characteristic strain curves for phase transition actuation. Although higher strain levels are achieved, these materials have very high hysteresis and therefore are good for applications where a memory effect is needed. However, these materials can not be used for low loss applications.

As with the piezoelectric PZT, these materials are lead based and therefore have the same processing limitations.

3.3. Single Crystal Relaxor Materials

Recently, relaxor type perovskite materials were demonstrated to exhibit exceptionally high levels of strain in single crystalline form. Materials such as $Pb(Mg_{1/3}Nb_{2/3})O_3$

(PMN) and $Pb(Zn_{1/3}Nb_{2/3})O_3$ (PZN) in solid solution with $PbTiO_3$ (PT) were grown by the flux method and were shown to have strain levels of up to 1.7% [12]. A comparison between the single crystal and polycrystalline materials is shown in Figure 4b. Recent work on non-lead materials showed that the $(Na_{1/2}Bi_{1/2})TiO_3$ - $BaTiO_3$ (NBT-BT) system exhibits strain levels of up to 0.85% [13].

One of the reasons for the high strain in the relaxor ferroelectrics is their rhombohedral crystal structure. The polarization for the rhombohedral phase is along <111> directions. Although the piezoelectric response along the <111> direction is not very strong, applying a field in a <100> direction can activate 4 equivalent dipoles. This improves the low field response in multi-domain materials. In addition, applying a sufficiently high field can result in a phase transition into the tetragonal phase, a transition that is accompanied by high strain (see Figure 3).

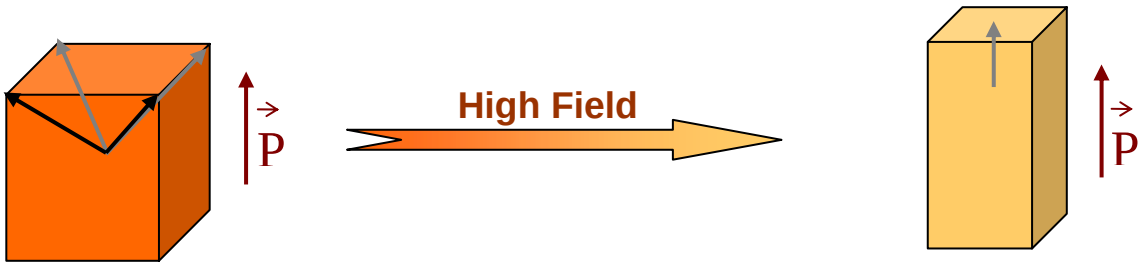

Figure 3: Schematic of the rhombohedral polarization and the phase transition that can occur at high electric field in the (001) direction.

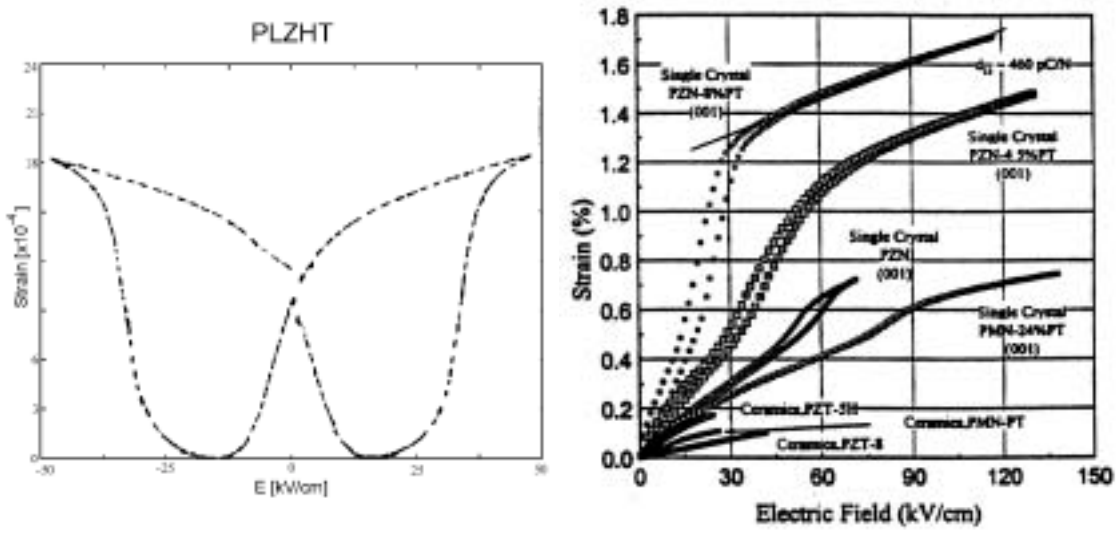

Figure 4: Strain - electric field plots showing (a) $Pb_{0.98}La_{0.02}(Zr_{0.7}Hf_{0.3})_{0.93}Ti_{0.07}O_3$ phase transition actuator, and (b) Comparison of single crystal and polycrystalline actuators. [10]

3.4. Piezoelectricity in $BaTiO_3$ systems

$BaTiO_3$ is one of the most extensively studied ferroelectric materials. It has a congruent melting point of 1612°C (see phase diagram in Figure 5), below which it has a hexagonal unit cell. Further cooling, below 1460°C, the structure becomes cubic perovskite, followed by transition into the tetragonal, monoclinic and rhombohedral at 130°C, 0°C, and -90°C respectively. The monoclinic unit cell can also be described in orthorhombic coordinates, rotated 90° around the c-axis. Details of the pseudo-cubic phases and their lattice constants are shown in Figure 5.

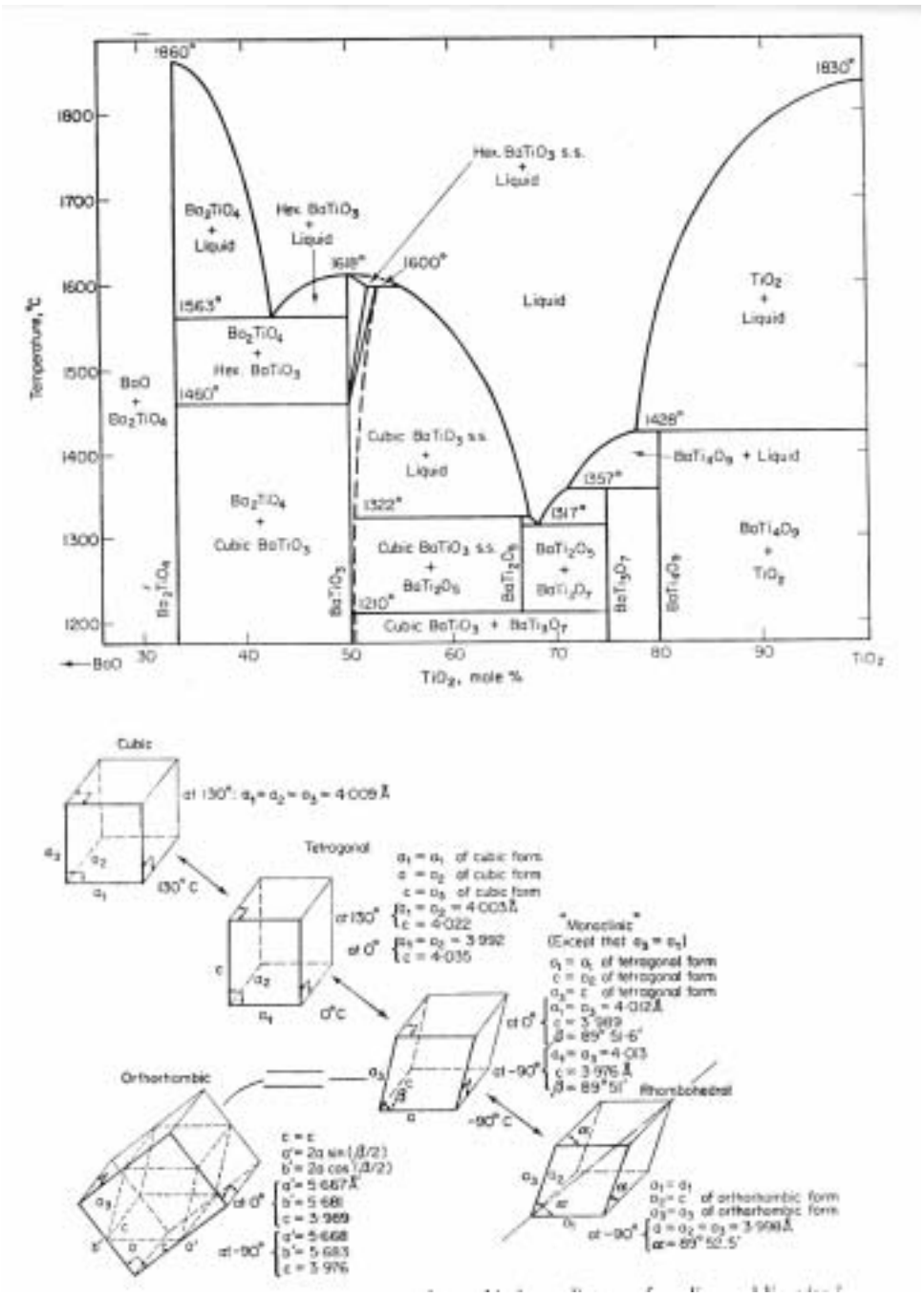

Figure 5: Phase diagram of the BaO-TiO_2 system and the ferroelectric transitions for $BaTiO_3$ at lower temperature. Although the basic unit cell at 0≥T≥-90°C is monoclinic, the equivalent orthorhombic cell is also shown. (From [14],[15])

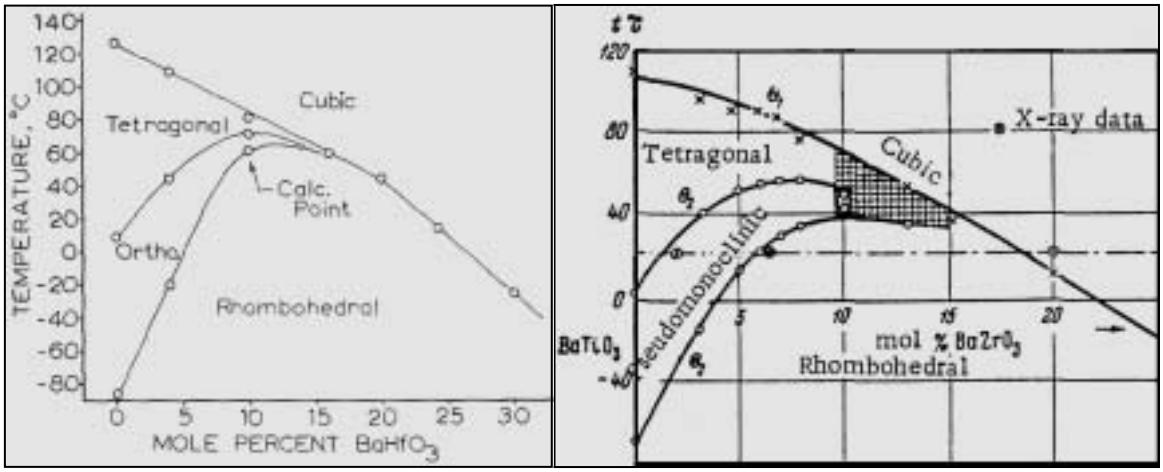

Figure 6: Phase diagrams for $BaTiO_3$:$BaHfO_3$ [16] and $BaTiO_3$:$BaZrO_3$ [17] showing a composition region where the rhombohedral phase is stable at room temperature.

$BaTiO_3$ based materials are of potential interest in a range of applications, including memory devices, tunable microwave dielectrics, and non-linear optics [18], [19]. The use of $BaTiO_3$ for piezoelectric applications is, however, limited due to the small piezoelectric coefficient of the room temperature-stable tetragonal phase [15]. In order to improve the piezoelectric response, efforts have been directed towards stabilizing the low-temperature rhombohedral phase. As has been mentioned in section 3.3, the rhombohedral structure can potentially have a higher piezoelectric response. The Goldschmidt tolerance factor for perovskites (t) describes the ratio of required spacing in the <110> and <100> lattice directions:

$$t = \frac{R_A + R_O}{\sqrt{2}\left(R_B + R_O\right)} \tag{13}$$

R_A, R_B, and R_O are the A-site, B-site, and oxygen ionic radii respectively. As a first approximation, t=1 corresponds to a perfect cubic structure, t>1 corresponds to tetragonal structure, and t<1 corresponds to a distorted cubic (monoclinic or rhombohedral). Generally speaking, one can increase the stability of the rhombohedral phase by increasing the size of the B-site ion. This, however, can also result in the lowering of the Curie point as the cubic phase becomes more favorable than the tetragonal one.

In $BaTiO_3$, the stabilization of the rhombohedral phase can be achieved through the addition of Zr, Hf, $KNbO_3$, and Sn. Figure 6 shows the phase diagrams for Zr and Hf doped $BaTiO_3$. Previous work has been done on some of these compositions for their dielectric properties [20]. Our work at MIT resulted in a patent on the use of the rhombohedral phase for its enhanced piezoelectric behavior [21]. Recent work by Rehrig *et al.*[22] indicates that single crystals of Zr doped $BaTiO_3$ maintain a piezoelectric coefficient of 480 pC/N even when highly porous, compared to 190 pC/N for the pure material.

4. Electro-optic Modulators

4.1. The Electro-optic effect

The 3D index of refraction can be described by the following elliptical surface:

$$\left(\frac{1}{n^2}\right)_1 x^2 + \left(\frac{1}{n^2}\right)_2 y^2 + \left(\frac{1}{n^2}\right)_3 z^2 + \left(\frac{1}{n^2}\right)_4 yz + \left(\frac{1}{n^2}\right)_5 xz + \left(\frac{1}{n^2}\right)_6 xy = 1 \qquad (14)$$

The notation above is the reduced notation, where 1=11, 2=22, 3=33, 4=23, 5=13, and 6=12. By transforming the tensor to its principle axes (for the case of no applied field this would be the crystallographic orientations) one gets a simple ellipse. Figure 7 shows such an ellipse with n_{11}, n_{22}, and n_{33} being the principle axes. Light propagating in the general direction S will see n_1 and n_2 as the 2 polarization indices. Materials for which the two polarization directions see a different index are called birefringent. The propagation velocity for light in matter (c) is related to the speed of light in vacuum (c_0) through the refractive index:

$$c = \frac{c_0}{n} \qquad (15)$$

For birefringent materials, the two polarizations will, therefore, propagate at a different velocity, resulting in rotation of the optical-polarization vector.

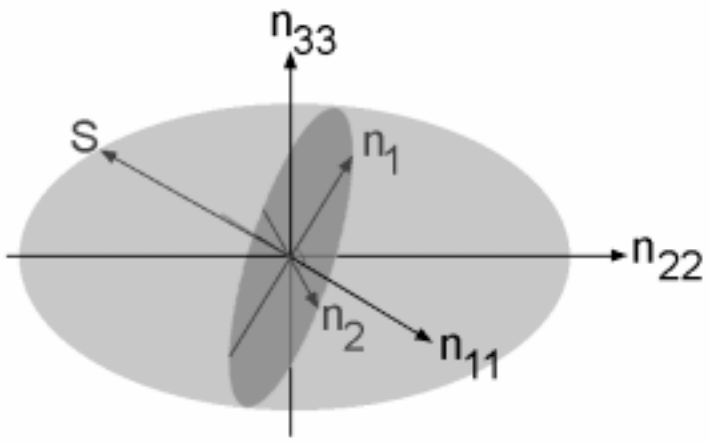

Figure 7: The index ellipsoid for the case of n_{11}, n_{22}, n_{33} as major axis indices. Light propagating in the S direction, will see two polarization components - one with index n_1 and the other with index n_2.

The electro-optic effect describes the change to the index ellipsoid due to an applied electric field (E):

$$\Delta\left(\frac{1}{n^2}\right)_i = r_{ij}E_j \qquad (16)$$

From symmetry considerations, the electro-optic tensor (r_{ij}) is limited in the number of independent components. For some of the common E-O symmetry systems these limitations are:

4mm (tetragonal): $r_{33}\neq 0$, $r_{13}=r_{23}$, $r_{42}=r_{51}$. Other $r_{ij} = 0$.

3m (trigonal / rhombohedral): $-r_{22}= r_{12}=r_{61}$, $r_{13}=r_{23}$, $r_{42}=r_{51}$. Other $r_{ij} = 0$.

Table 2 on page 30 contains some specific values for the electro-optic coefficients of $BaTiO_3$, $LiNbO_3$ and some other commonly used materials.

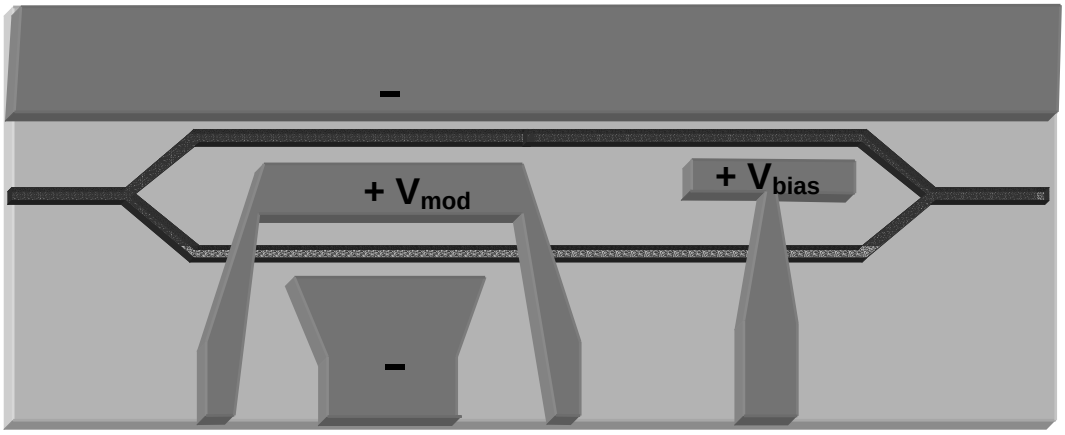

Figure 8: Schematics of a Mach-Zender modulator. Light propagates from the right, through a bias field and then through the modulating field.

4.2. $BaTiO_3$ for electro-optic applications

Electro-optic modulators translate an electric signal to an amplitude modulation of a light signal. The most common type of modulator is the Mach-Zender modulator, shown schematically in Figure 8 [23]. A signal traveling in an electro-optic waveguide is split into two branches. Each branch is then subjected to a different electric field, resulting in a different refractive index. The difference in refractive index creates a phase mismatch between the two branches as they recombine, affecting the output intensity. The length of the device depends on the change in refractive index that can be achieved. A high electro-optic response is therefore required for miniaturization. In addition, the characteristic length of these devices is 0.1-10mm, making it essential to have low loss waveguides. Maximum loss of 1-3dB per device is usually accepted, requiring material losses of several dB per cm.

$LiNbO_3$ is the commonly used material for electro-optic modulators. This is largely due to the ability to grow $LiNbO_3$ as large, high quality single crystals. However, the electro-optic coefficient of $LiNbO_3$ is low compared to many other ferroelectric materials. In addition, it is of growing interest to integrate optical components with the electronics on the same chip. This requires materials compatible with current silicon technology.

$BaTiO_3$ has a high electro-optic coefficient, r_{42}~820. In addition, the simple cubic structure of $BaTiO_3$ can be grown on Si using buffer layers of MgO[24], TiN[25] and

Ni/NiO[26]. Most work to-date on the integration of $BaTiO_3$ on Si has been for dielectric applications. Similar research on $BaTiO_3$ for integrated optics applications remains sparse.

For tetragonal $BaTiO_3$ the index ellipsoid can be written in terms of principle axes using $n_{11}=n_{22}=n_o$ and $n_{33}=n_e$:

$$\left(\frac{1}{n_o^2}\right)x^2+\left(\frac{1}{n_o^2}\right)y^2+\left(\frac{1}{n_e^2}\right)z^2=1 \tag{17}$$

The electro-optically modified index ellipsoid is given by:

$$\left(\frac{1}{n_o^2}+r_{13}E_z\right)x^2+\left(\frac{1}{n_o^2}+r_{13}E_z\right)y^2+\left(\frac{1}{n_e^2}+r_{33}E_z\right)z^2+2r_{42}E_x yz+2r_{42}E_y xz=1 \tag{18}$$

For an electric field in the z direction (tetragonal c-axis) the principle directions are left unchanged, but their magnitude is modified:

$$\frac{1}{n'^2_o}=\frac{1}{n_o^2}+r_{13}E_3 \text{ and } \frac{1}{n'^2_e}=\frac{1}{n_e^2}+r_{33}E_3 \tag{19}$$

Assuming small changes in the index and using:

$$dn=-\frac{n^3}{2}d\left(\frac{1}{n^2}\right) \tag{20}$$

Both forms of equation (19) can be written as:

$$n'_i=n_i-\frac{n_i^3}{2}r_{i3}E_z \text{ (i = 1,2 for } n_o \text{ and 3 for } n_e)$$

For electric field in the y direction, the calculation is more complicated:

$$\left(\frac{1}{n_o^2}\right)x^2+\left(\frac{1}{n_o^2}\right)y^2+\left(\frac{1}{n_e^2}\right)z^2+2r_{42}E_y xz=1 \tag{21}$$

The mixed component xz implies rotation of the principle axis directions. The amount of rotation (θ) depends on the magnitude of the electro-optic change compared to the birefringence of the material. Two limiting cases are:

$$r_{42}E << \left|\frac{1}{n_e^2} - \frac{1}{n_o^2}\right| \tag{22}$$

$$r_{42}E >> \left|\frac{1}{n_e^2} - \frac{1}{n_o^2}\right| \tag{23}$$

The magnitude of the change is, in both cases:

$$n'_x = n_o + \frac{n_o^3}{2} r_{42} E_y \ , \ n'_y = n_o \ , \ n'_z = n_e - \frac{n_e^3}{2} r_{42} E_y \tag{24}$$

By observing similar approximations for other orientations, one can define a figure of merit:

$$F.O.M = n_i^3 r_{jk} \tag{25}$$

The figure of merit in equation (25) defines the magnitude of an index change for a given electric field. Comparison of the F.O.M of $BaTiO_3$ and $LiNbO_3$ is given in Table 2, together with the values for the electro-optic coefficient and the index of refraction. These values show the advantage of using $BaTiO_3$ for E-O applications.

Table 2: Comparison of the figure of merit, n^3r, for some electro-optic materials. Based on data from Holman *et al.* [27]

Material	ε (1GHz)	r_{ij} [m/V]	n_o	n_e	film	field	n^3r
$BaTiO_3$	372	r_{13}=8, r_{33}=23, r_{42}=820	2.437	2.365	c c	z y	334 10,850
$LiNbO_3$	37	r_{13}=8.6, r_{22}=3.4 r_{33}=30.8, r_{42}=28	2.29	2.20	c a a	z y z	328 37 113
PLZT	1285	r_c=136	2.5		c	z	2,125
$KNbO_3$	137	r_{33}=64, r_{42}=380	2.25	2.17	c c	z y	653 4,328
GaAs	14	r_{42}=1.2	3.6	3.6	c	z	56
InP	14	r_{42}=1.5	3.21	3.21	c	z	50

From the data described so far, it has been demonstrated that $BaTiO_3$ has superior bulk properties compared to $LiNbO_3$, and is more compatible with Si technology. Other promising systems, such as $KNbO_3$ and PLZT, have been studied elsewhere [28],[29]. Of all these systems, however, $BaTiO_3$ has the highest potential in terms of bulk properties. There are, however, several problems related to the integration of $BaTiO_3$ onto Si.

The high electro-optic coefficient is limited to the off-diagonal r_{42} component. This can introduce rotation and polarization mixing. For example, one can consider the simple case of a (001) oriented film. The z direction is taken to coincide with the extraordinary index, perpendicular to the surface, and the field is applied in the x direction, parallel to the surface (see Figure 9). The index ellipsoid is reduced to:

$$\frac{x^2}{n_o^{\,2}} + \frac{y^2}{n_o^{\,2}} + \frac{z^2}{n_e^{\,2}} + 2r_{42}E_x xz = 1 \tag{26}$$

The ellipsoid is rotated around the y axis by an angle θ, given by:

$$\tan 2\theta = \frac{2r_{42}E_x}{\frac{1}{n_o^{\,2}} - \frac{1}{n_e^{\,2}}} \tag{27}$$

The index of refraction in the new orientation x' and z' are:

$$\begin{aligned} n_{x'} &\cong n_o - \frac{1}{2}n_o^{\,3}r_{42}E_x \tan\theta \\ n_{z'} &\cong n_e + \frac{1}{2}n_e^{\,3}r_{42}E_x \tan\theta \end{aligned} \tag{28}$$

The results in (27) and (28) emphasize the importance of the birefringence. For small values of birefringence, the angle θ is close to 45°, and the electro-optic effect is maximized.

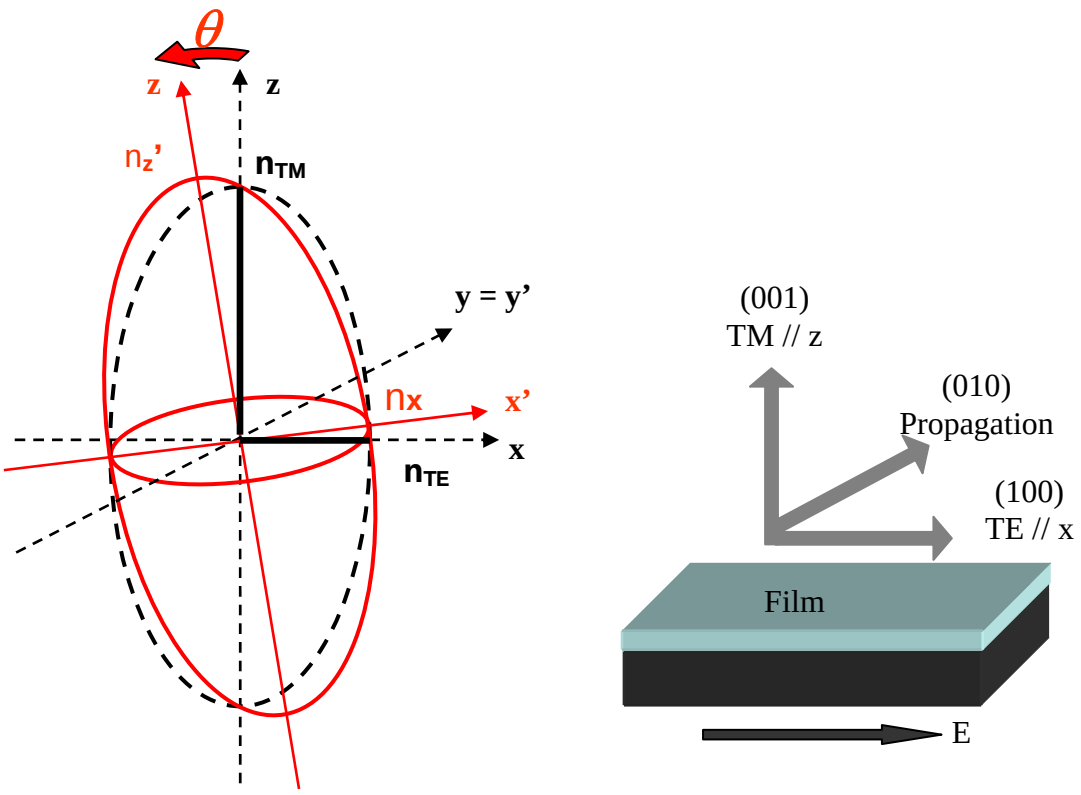

Figure 9: Index ellipsoid and the polarization rotation for the case of (001) film and (100) field (illustrated on the right).

For larger values of birefringence, θ decreases rapidly, and with it the electro-optic response. Taking a small angle approximation of $tan\theta \sim \theta$, one can re-write equation (28) as:

$$n_{x'} \cong n_o - \frac{1}{2} n_o^{\,3} r_{42} E_x \cdot \frac{r_{42} E_x}{\frac{1}{n_o^{\,2}} - \frac{1}{n_e^{\,2}}} = n_o - \frac{1}{2} n_o^{\,3} \left(r_{42} E_x\right)^2 \frac{n_e^{\,2} n_o^{\,2}}{n_e^{\,2} - n_o^{\,2}}$$

$$n_{z'} \cong n_e + \frac{1}{2} n_e^{\,3} r_{42} E_x \cdot \frac{r_{42} E_x}{\frac{1}{n_o^{\,2}} - \frac{1}{n_e^{\,2}}} = n_e + \frac{1}{2} n_e^{\,3} \left(r_{42} E_x\right)^2 \frac{n_e^{\,2} n_o^{\,2}}{n_e^{\,2} - n_o^{\,2}} \qquad (29)$$

An interesting result from equation (29) is that for the birefringent material, the change in index depends on the field squared, rather then the standard linear dependency.

From the above discussion, it is evident that the orientation of the $BaTiO_3$ film is very important. Several buffer layers have been suggested for the oriented growth of $BaTiO_3$

on Si. Most common are MgO, (Sr,Ba)O, CeO_2 and TiN [25]. Of these materials, MgO has been studied the most as a substrate for $BaTiO_3$, mostly due to the high lattice matching and the low thermal expansion coefficient mismatch [30]. The refractive index of $BaTiO_3$ is lower then that of the Si substrate. This can result in optical losses unless a buffer of at least 2μm is used. This becomes an issue since the growth rate of MgO is limited to around 100nm/hr [31]. Recently, the deposition of oriented $SrTiO_3$ on SOI was reported by Eisenbeiser et al. [32] from Motorola. A similar technique might be possible for growing $BaTiO_3$ on Si with a thick buffer layer. During the growth process described by Eisenbeiser et al., the top Si layer is oxidized. This would result in a volume increase of that layer, and possibly dislocation formation due to that. For our devices, however, a low density of dislocations should not pose a problem. As long as the dislocation density is much smaller then $1/\lambda^2$ (for $\lambda \sim 1.5\mu m$, $\rho < 10^{-8}$ cm-^{2}) the effect on the optical properties should remain small. Furthermore, $BaTiO_3$ can form pure edge {101}/<101> dislocation systems at the growth interface in order to accommodate lattice mismatch [33]. This ensures a low density of dislocations in the bulk.

The high dielectric constant of $BaTiO_3$ compared to that of the surrounding material (MgO or SiO_2) makes it difficult for the electric field to penetrate into the waveguide. The field distribution for the case of $BaTiO_3$ surrounded by MgO on a Si/SiO_2 wafer is shown in Figure 10. The fact that the electric field does not penetrate the $BaTiO_3$ effectively lowers the electro-optic coefficient.

Addition of Zr to $BaTiO_3$ has been reported to reduce the RF dielectric constant. In addition the addition of Zr and Hf increase the lattice parameter of $BaTiO_3$, therefore reducing the lattice mismatch with MgO[34]. The reduction in lattice mismatch could allow for a lower processing temperature.

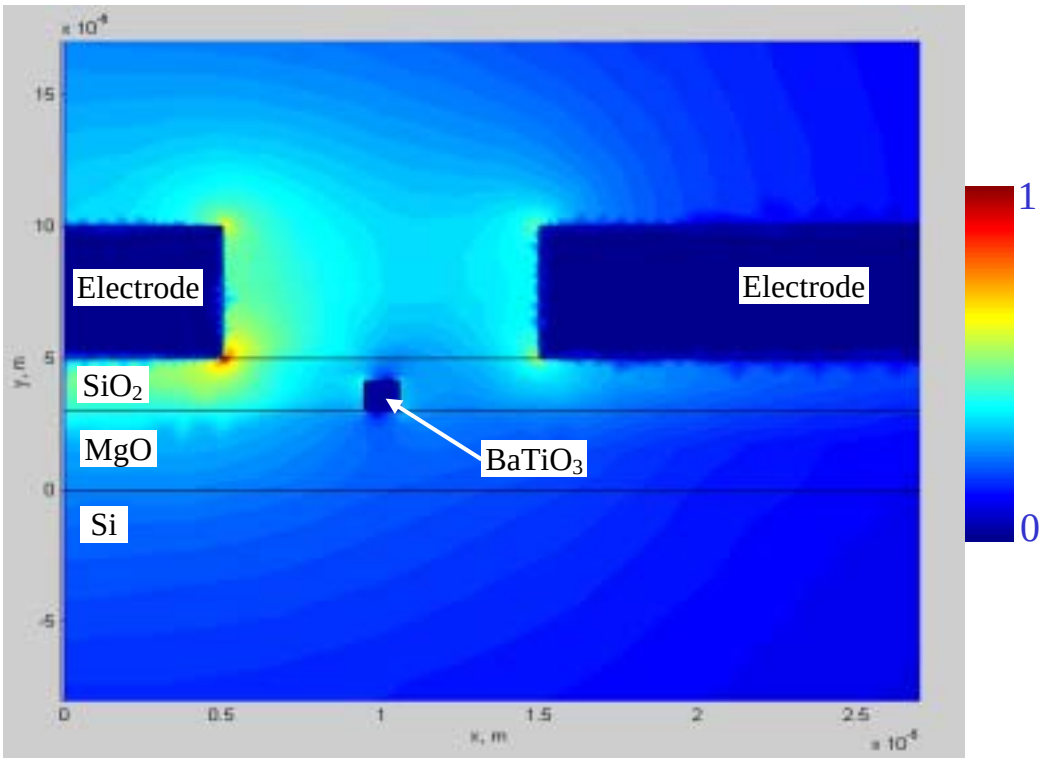

Figure 10: Electric field distribution in a $BaTiO_3$ buried waveguide. The field does not penetrate the high dielectric region of the $BaTiO_3$. Calculated by Luciano Socci, Pirelli Labs, Milan.

Chapter 2: Objectives

The major objectives of this research were:

(1) To stabilize the rhombohedral phase of $BaTiO_3$ at room temperature and to study its piezoelectric properties

(2) To study the optical properties of $BaTiO_3$-based films and their dependence on deposition conditions

1.1. Bulk Materials

Zr, Hf, and KNb were chosen as candidate materials for stabilizing the rhombohedral phase. Samples of different composition were prepared and studied by x-ray diffraction in order to investigate the phase stability region. Dielectric measurements as a function of temperature were carried out and analyzed to find the phase transition temperatures. Piezoelectric measurements were carried out in order to extract the piezoelectric constant and maximum strain.

1.2. Thin Films

Three compositions were chosen for deposition, pure $BaTiO_3$, 8%Zr:$BaTiO_3$, and 10%Hf:$BaTiO_3$. The three compositions have different lattice parameter and, therefore, different lattice mismatch with the substrate. The hypothesis was that lowering the lattice mismatch can help reduce the strain in the film and lower the growth temperature. In order to check this hypothesis, x-ray analysis was used to characterize crystallographic orientation and strain in the films. This was done at different growth conditions and analyzed for trends.

The index of refraction was measured using ellipsometry and transmission perpendicular to the film was used to ensure low losses. The objective was to correlate the refractive index with growth conditions and film parameters. Since the Curie temperature for these materials is low, ranging from 35°C for 8%Zr:$BaTiO_3$ to 130°C for pure $BaTiO_3$, thermal dependency of the optical properties is very important for device performance. The temperature dependency of the refractive index was measured, as was thermal stability after low temperature anneal.

Chapter 3: Experimental

This section describes the sample preparation and characterization methods used in this research.

1. Sample Preparation

1.1. Polycrystalline Samples

Polycrystalline samples were prepared by solid-state reaction of precursor materials. Barium carbonate and potassium carbonate were used as sources for the A-site and metal oxides for the B-site ions. The desired molar ratio of powders was measured, and then ball milled and sieved to ensure small particle size. Powders were then pressed into pellets at 5000 psi, reacted at T~700°C and sintered at T~1200°C. The pellets were then ground, mixed, and sieved to achieve maximum uniformity and avoid porosity related to the solid state reaction. The powders were then uniaxially pressed at 7000psi, followed by iso-pressing at 40000 psi, and sintering at a higher temperature. A characteristic time-temperature sintering curve is shown in Figure 11. The pellets were held at 650°C to ensure complete binder burn-out prior to sintering at a temperature of 1300-1450°C. A list of sample compositions and the corresponding sintering conditions are given in Table 3.

Table 3: Polycrystalline sample compositions and sintering conditions.

Composition	x [%mol]	Sintering conditions
$Ba(Ti_{1-x}Zr_x)O_3$	7-15	3-4 hrs, 1400°C
$Ba(Ti_{1-x}Hf_x)O_3$	9-15	3-4 hrs, 1400-1450°C
$(BaTi)_{1-x}(KNb)_xO_3$	3.8, 4, 6	3 hrs, 1300°C

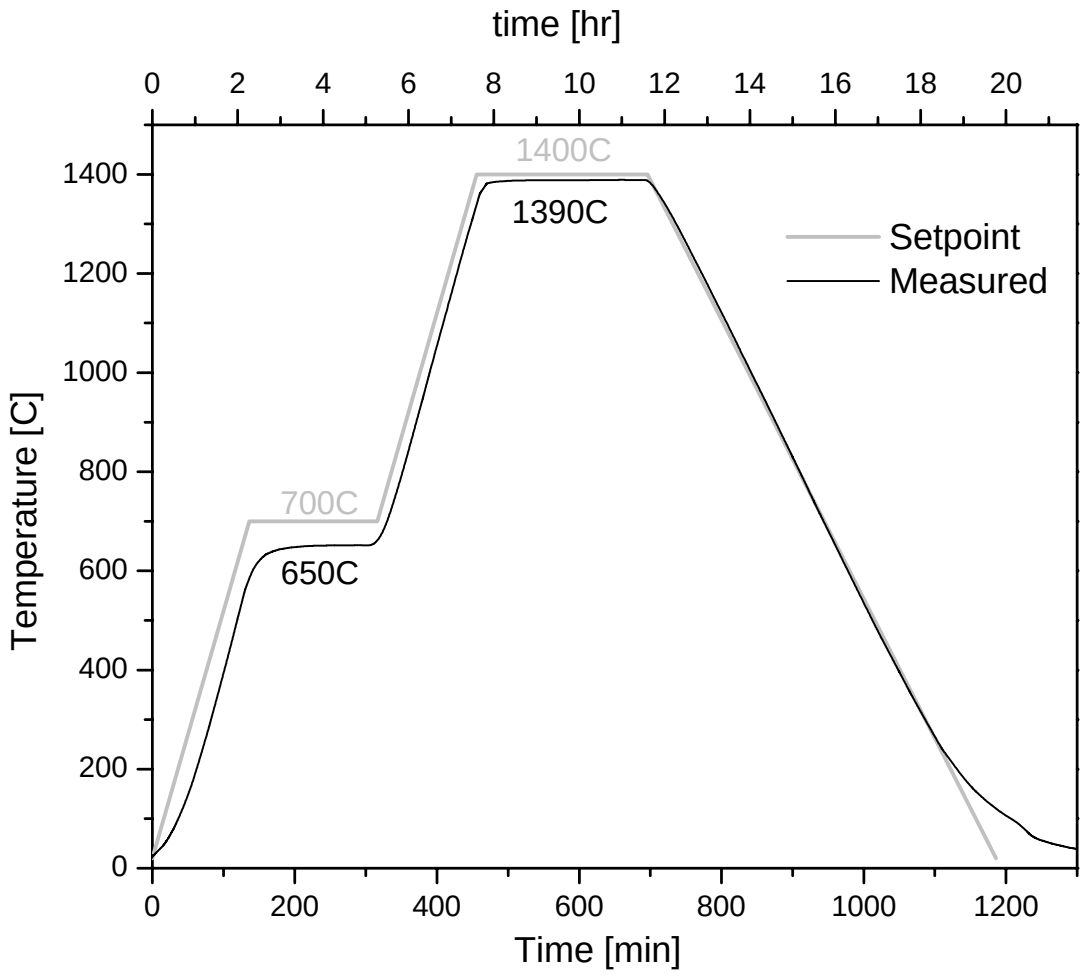

Figure 11: A characteristic time – temperature profile for sintering as measured in the furnace compared to the set-point.

1.2. Pulsed Laser Deposition (PLD)

$BaTiO_3$ films were grown using a Pulsed Laser Deposition system. A Lambda Physik LPX325i laser source with λ=248nm was used. A schematic drawing of the PLD system is shown in Figure 12. A lens is used to focus the laser beam onto the target surface, which gives a fluency of up to 7 J/cm^2. The high energy of the beam results in a plume of material being emitted and deposited on the substrate. The laser beam scans the target in order to reduce local damage to the target. The scanning is performed by moving the focusing lens, therefore moving the focal point. A heater unit is used to heat the substrate for growth at elevated temperatures.

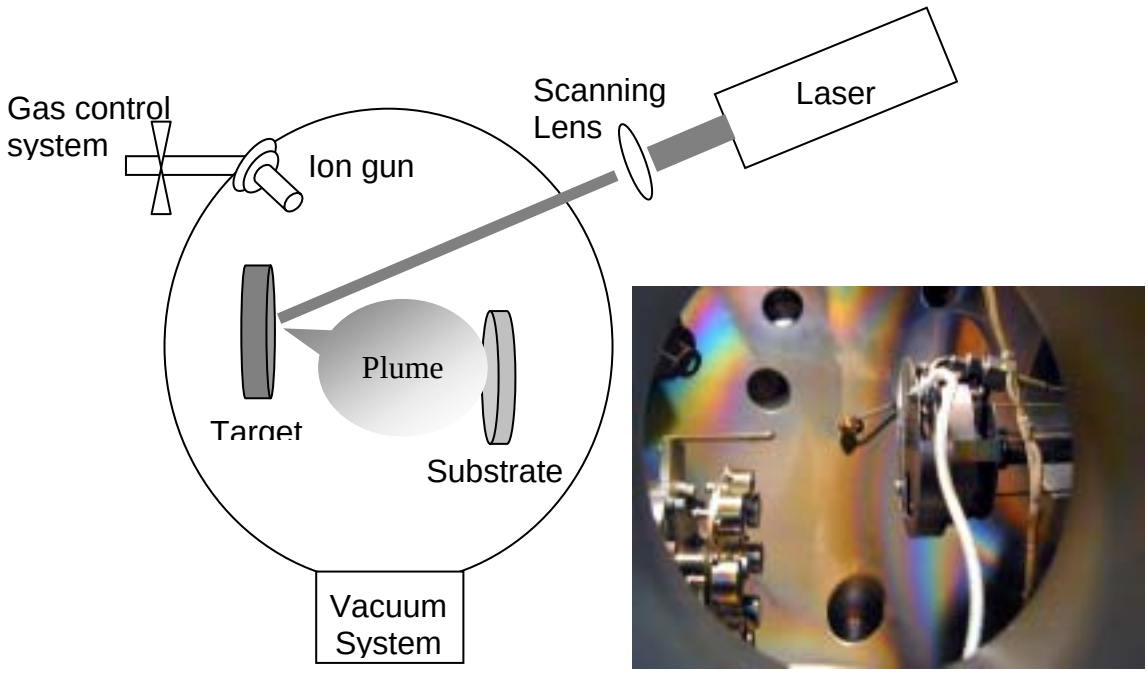

Figure 12: Schematic drawing of the PLD system. The insert shows a photograph of the deposition chamber with the targets on the left and substrate on the right.

Targets for the PLD were made using the technique described in section 1.1 above. The polycrystalline target surface was cleaned using acetone, followed by laser ablation in the PLD. After 20,000 pulses at 3 J/cm^2, the target was ready for deposition.

Single- and double-sided polished MgO substrates were obtained from MTI Crystals, Inc. To investigate the effect of magnesium hydroxide surface layers, some substrates were heat treated in air for 1 hour at 700°C, and for 3 hours at 850°C. Ion bombardment of the surface was also investigated, using the in-situ ion gun in the PLD system. Both of these surface treatments did not affect either film orientation or film quality. A list of deposition conditions is given in Table 4.

The deposition of oriented $SrTiO_3$ on SOI was reported by Eisenbeiser et al [32]. A similar process was examined for the growth of $BaTiO_3$. SOI wafers were obtained from SOITECH. The native oxide was removed from the top Si layer using an HF etch. A thin layer of MgO was deposited in vacuum, to prevent the re-oxidation of the Si. Once an oriented MgO seed layer was obtained, the chamber was flooded with oxygen at 700°C for 30 min to achieve oxidation of the top Si layer. The process can be seen in Figure 13.

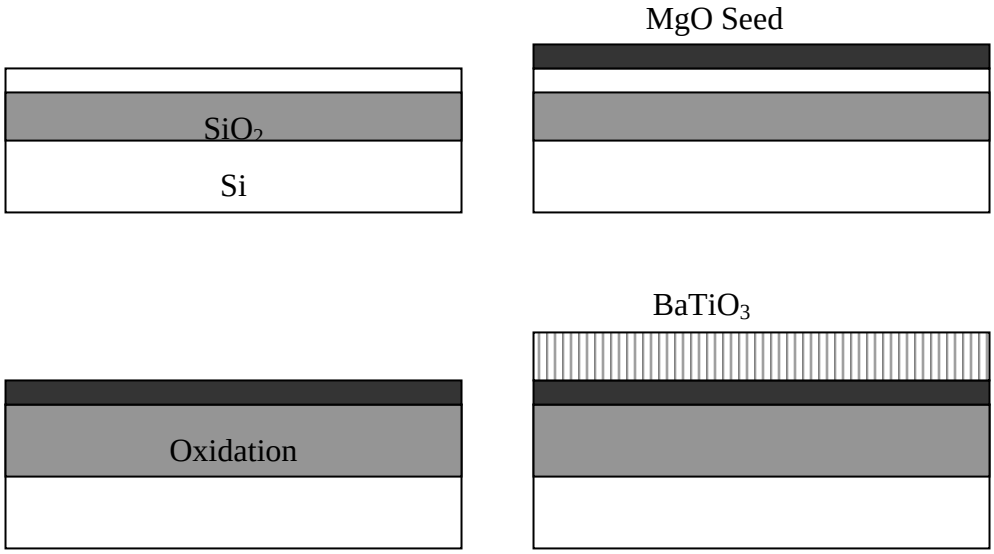

Figure 13: Schematic representation of the growth of $BaTiO_3$ on SOI. See text for details.

Table 4: PLD deposition conditions

Property	Temperature	Fluency	Composition	Environment	Pressure
MgO Substrate	500-725°C	2-5 J/cm^2	Pure, 8%Zr, 10%Hf	Vacuum, 1:1 Ar:O_2, O_2	10^{-6} – 10^{-2} Torr
SOI Substrate	650-725°C	4-5 J/cm^2	Pure, 10%Hf	O_2	10^{-2} Torr

1.3. RF Sputtering

MgO films were grown using an RF sputtering system. A schematic description of the sputtering system is shown in Figure 14. 2" MgO targets, 99.99% purity were obtained from Kurt Lesker. The system was pumped down to $P<1\cdot10^{-6}$ [Torr] and the appropriate gas mixture was introduced. Ar-O_2 compositions between 75-100% Ar were used. The substrate was heated using a halogen heater to 400°C, and was rotated during deposition to increase homogeneity.

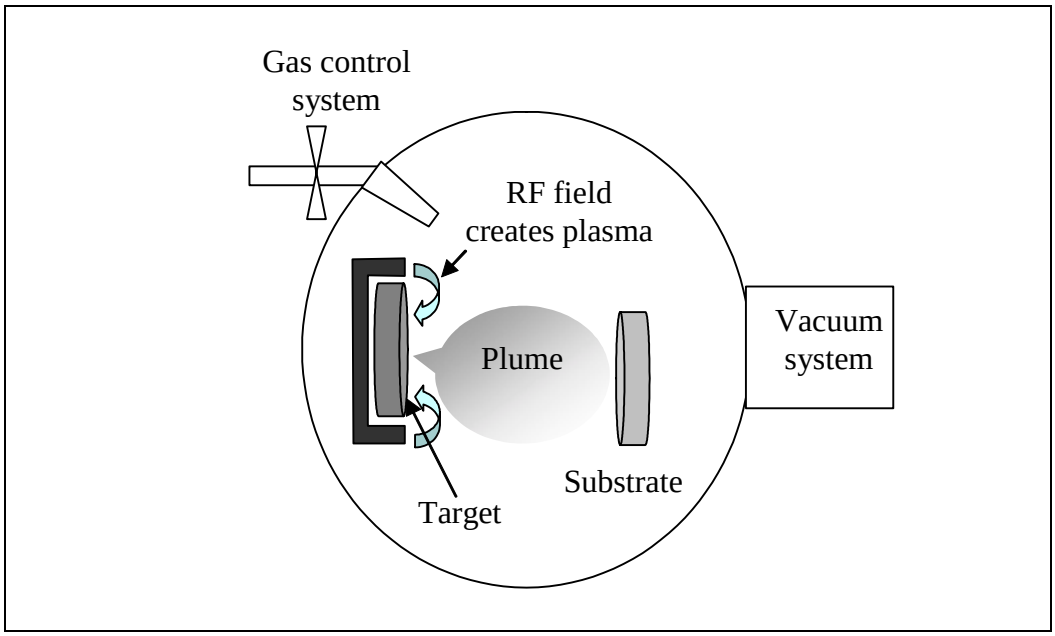

Figure 14: Schematic drawing of the RF sputtering system

2. Characterization

2.1. X-ray Analysis

Powder X-ray Diffraction (XRD) is commonly used for structure and phase analysis. During cooling from the paraelectric phase, the crystalline symmetry of $BaTiO_3$ decreases. The result is splitting of the once degenerate cubic diffraction peaks. For the tetragonal phase the {100} peaks become {100} and {001} while for the rhombohedral phase the $\{111\}$ splits into $\{111\}$ and $\{11\bar{1}\}$.

In thin films, oriented growth can result in fewer diffraction peaks. In the case of full epitaxial growth, only one family of diffraction peaks will be visible in the diffraction pattern. If the films are not fully oriented, other diffraction peaks will start to show and their relative intensity can teach us about the level of orientation.

Three X-ray setups were used to characterize the bulk and film samples. The standard Bragg-Brentano configuration was used for the polycrystal samples and for samples with low levels of orientation. Since the number of diffraction peaks and their intensity were not always sufficient to characterize the films, an additional measurement was conducted using a thin film setup (Figure 15). A glancing incident beam, usually less then 1° to the surface is used to illuminate the film. Due to the small angle, most of the x-ray intensity is confined in the film and the diffraction signal is enhanced. The detector is then moved along 2θ and the intensity is recorded. Unlike the standard Bragg diffraction, the reflecting planes in this case are not parallel to the surface, allowing for more peaks to be recorded even in oriented films. This setup can help in cases of low level of orientation, but is still limited when higher epitaxial relations occur.

For high level of orientation, a high resolution X-ray diffraction system was used (Figure 16). The system uses a four crystal monochromator to collimate the beam, a process resulting in higher accuracy in the diffraction pattern. The system can scan the stage and the detector in a θ-2θ configuration. In addition, it is possible to offset the sample from the Bragg conditions. The offset to θ is called an ω-scan.

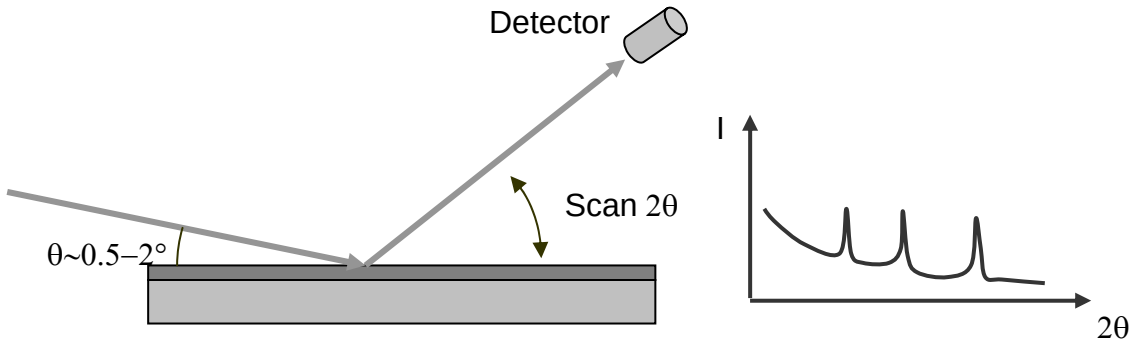

Figure 15: Thin film setup for X-ray diffraction. See details in the text.

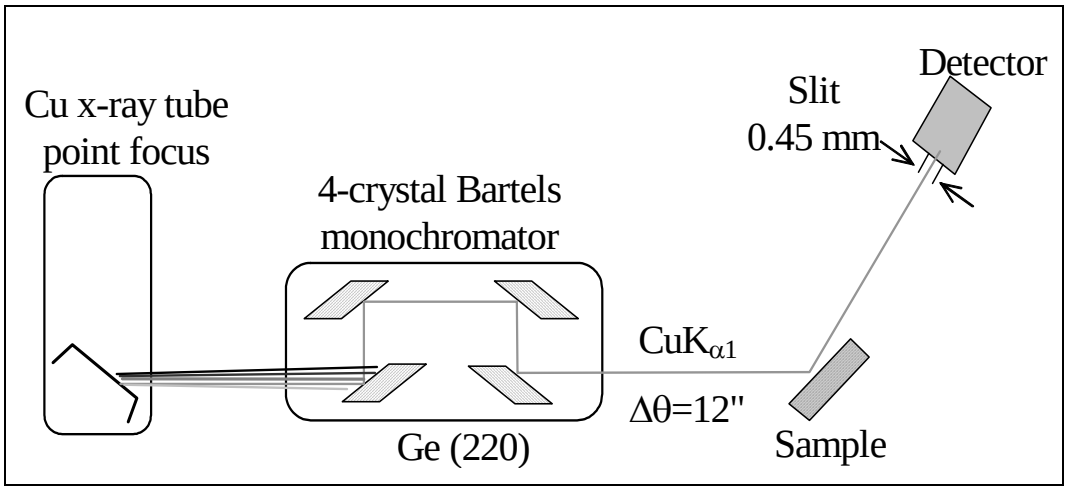

Figure 16: Schematic representation of the high resolution X-ray diffraction system. See text for details.

2.2. Microstructure Analysis

Optical microscopy is a very useful technique for characterizing polar materials. Polarized light can be used to enhance the visibility of domain structure and defects. For higher magnifications, electron microscopy is needed. The use of a field emission gun high-resolution scanning electron microscope (FEG-HRSEM) allows the use of low working potentials. This is important in non-conductive materials as it reduces charging effects. Consequently, a larger magnification image can be achieved without coating the sample. Another advantage of using electron microscopy is the ability to use wavelength dispersion spectroscopy (WDS). WDS uses the characteristic X-ray emission lines to evaluate sample composition. The combination of WDS with bright field image can be used to find composition inhomogeneities and relate them to regions within the material.

2.3. Thickness Measurements

Sample thickness was measured using profilometry (Tencor P10 Surface Profiler) and ellipsometry (Gaertner Scientific variable angle ellipsometer, λ=633nm), the two techniques complementing each other. Profilometry is limited to the edges of the film, and therefore can have inaccuracies when the substrate is not flat all the way to the edge. Ellipsometry, on the other hand, gives accurate measurements at the center of the sample. Since the ellipsometry measurement depends on interference effects from the top and

bottom of the film, it gives a set of results for the thickness. This set has a periodicity that depends on the refractive index, the thickness and the incident angle. Choosing the correct thickness from the set is possible by using the values measured in the profilometer. A schematic diagram of how these measurements were taken is shown in Figure 17.

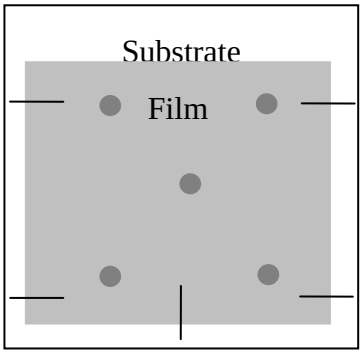

Figure 17: Schematic drawing showing the profilometry scans (lines) and ellipsometry measurements (circles) used to obtain film thickness.

2.4. Index of Refraction Measurements

A Metricon 2010 system was used to measure the ordinary and extraordinary indices of $BaTiO_3$ films. A schematic of the system is shown in Figure 18. A laser beam is focused onto the surface of the sample, using a coupling prism. The beam is scanned at an angle smaller than the external reflection condition (θ_B) so that the full intensity is reflected from the surface, and the intensity is recorded at the detector. If a propagating mode exists in the film, light will couple into it and a lower intensity is registered at the detector. By analyzing the mode angles, one obtains the index of refraction for the film. The incoming beam can be polarized either parallel or perpendicular to the film in order to obtain both TE and TM data.

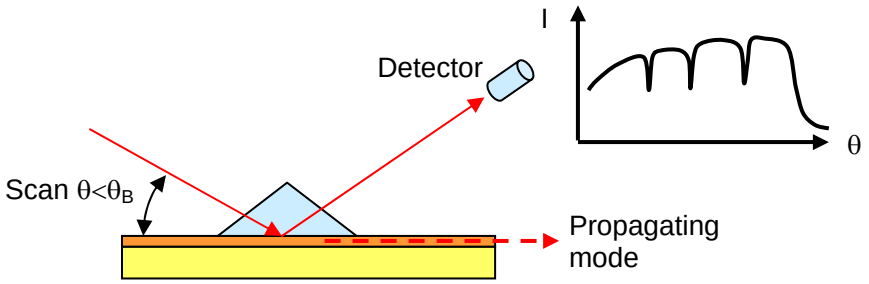

Figure 18: Schematic drawing of the Metricon system. See text for details.

2.5. Electron Microscopy and Chemical Analysis

Electron microscopy was performed using two systems: a high resolution FEG-SEM, and an EPMA enabled system.

A JEOL 6320FV Field-Emission High-resolution SEM was used to obtain back scattered and secondary electron images. The system is equipped with a field emission gun and an in-column detector, allowing for a lower acceleration voltage and a shorter working distance. This allows working with insulating materials without a conductive coating, although at higher magnifications charging can still occur. Standard working conditions were 1-3kV at 2-3mm for secondary electrons, and 8kV at 8mm for back-scattered imaging. The microscope is also capable of Energy Dispersive Spectrometry (EDS) for chemical analysis, however the emission lines of the different components in the system are too close together and little information could be obtained.

A JEOL JXA-733 Electron Microprobe (EMP), also known as the Electron Probe X-ray Microanalyzer (EMPA), was used to obtain images and chemical analysis for both bulk and thin films. X-ray emissions, resulting from the e-beam interaction with the sample, are measured by Wavelength Dispersive Spectrometry (WDS). Unlike EDS, which collects the total emission from all the elements in the sample, WDS utilizes a directional detector that needs to be positioned for each element of interest. The result is a much more accurate value for the specified element, especially when compared to a standard, however, it makes for a much slower scan and is limited to a small set of elements.

2.6. Piezoelectric measurements

Electromechanical measurements were performed using a laser interferometery method. The system is illustrated schematically in Figure 19. The beam reflected from the sample is compared to the one that comes directly from the beam-splitter. The Doppler shift is translated into velocity, which is in turn integrated to calculate translation. Information from the power supply and from the optical system is fed into a computer where the actual field and strain are calculated. The sample sits in an oil bath, which enables temperature control either during measurement or for poling. A detailed description of the system and its components can be found in [35].

Samples were tested prior to poling. Figure 20 shows the current vs. field plot prior to poling. The field at which domain motion begins is characterized by a sharp peak in current, as can be seen for the Zr-doped sample around 5kV/cm. Even when such a peak was not seen, an increase in the slope of the current around 10kV/cm was observed, suggesting an increase in domain motion. From these measurements, a poling field of 10kV/cm was chosen. The poling was performed by cooling through the Curie temperature at 0.5°C/min under an applied electric field. A 1kV/cm ac signal was added to the 10kV/cm dc signal in order to improve the poling process [36].

The piezoelectric measurements were carried out in two modes: hysteresis loop and d_{33} measurement. In hysteresis loop mode an AC voltage of -V to +V is applied on the sample, which allows the observation of domain switching. In d_{33} mode an AC voltage of 0 to +V is applied, to reduce the hysteresis. The voltage amplitude was increased at steps of 0.5kV until dielectric breakdown occurred. A piezoelectric measurement was performed at each step, with the value from the last step prior to breakdown being taken for maximum strain. All the piezoelectric measurements were done at 1Hz and after the sample had sufficient time to cool from the poling process to below 25°C.

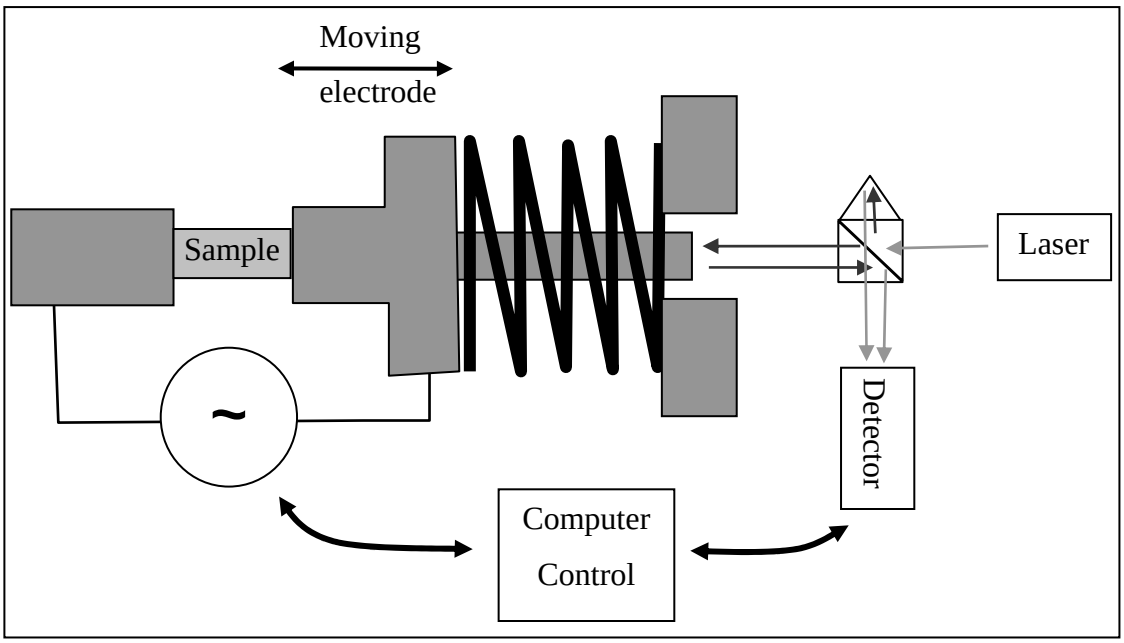

Figure 19: Schematic of the electro-mechanical testing system.

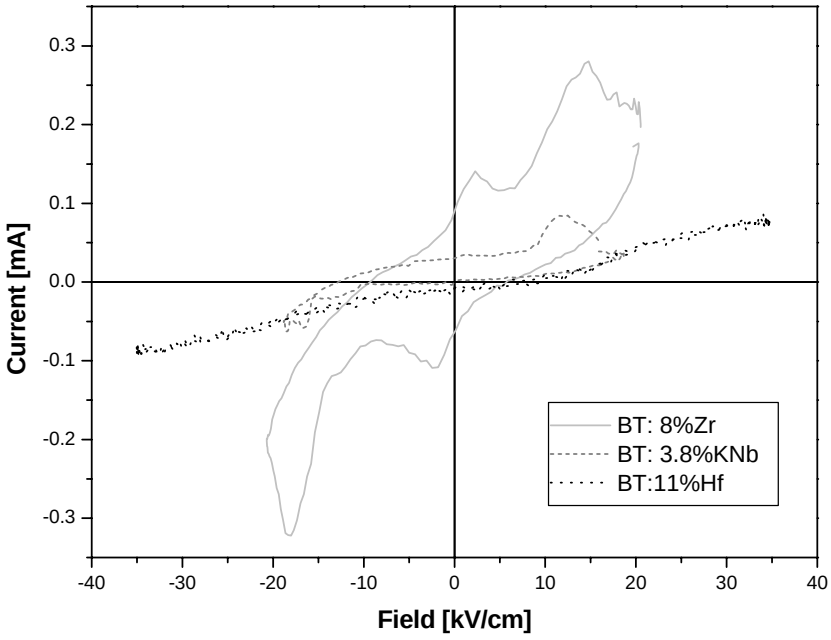

Figure 20: Current vs. Field plot for samples prior to poling.

Chapter 4: Results

1. General

This chapter includes the experimental results for both the bulk and thin-film samples. As appropriate, limited analysis of the data is presented here. The major part of the data analysis is left to Chapter 5: Discussion.

The results are split into two main categories – the bulk-polycrystal, and the thin film data. Each of those categories is further divided according to the nature of the experiment.

2. Poly-Crystal Samples

2.1. X-ray

X-ray diffraction spectra of "as-prepared" samples showed either tetragonal, rhombohedral or both phases. An example is shown in Figure 21, where both the (111) rhombohedral split and the (200) tetragonal split are visible in $BaTiO_3$ with 3.8%$KNbO_3$. It is important to note that although different morphologies can co-exist, the samples did not reveal the presence of any minor phases.

Applying even a small poling field (as low as 1kV/cm) reduced the stability of the tetragonal phase and X-ray spectra taken after poling show only the rhombohedral (111) split, as can be seen in Figure 22 and Figure 23. The fitted peak patterns were obtained using Origin [37].

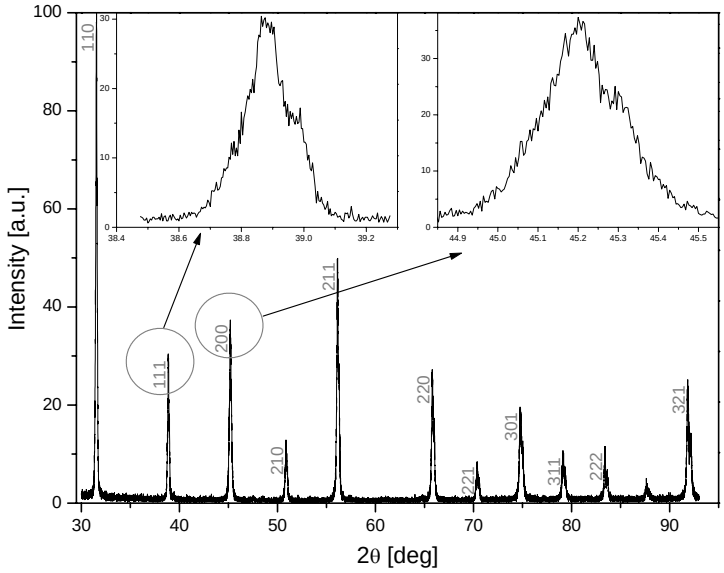

Figure 21: X-ray diffraction spectrum for $BaTiO_3$ with 3.8% $KNbO_3$ as sintered. The main graph shows peak matching the $BaTiO_3$ phase, while the inserts zoom in on the (111) and (200) peaks. Peak splitting in both suggests that both the tetragonal and the rhombohedral phases coexist in the sample.

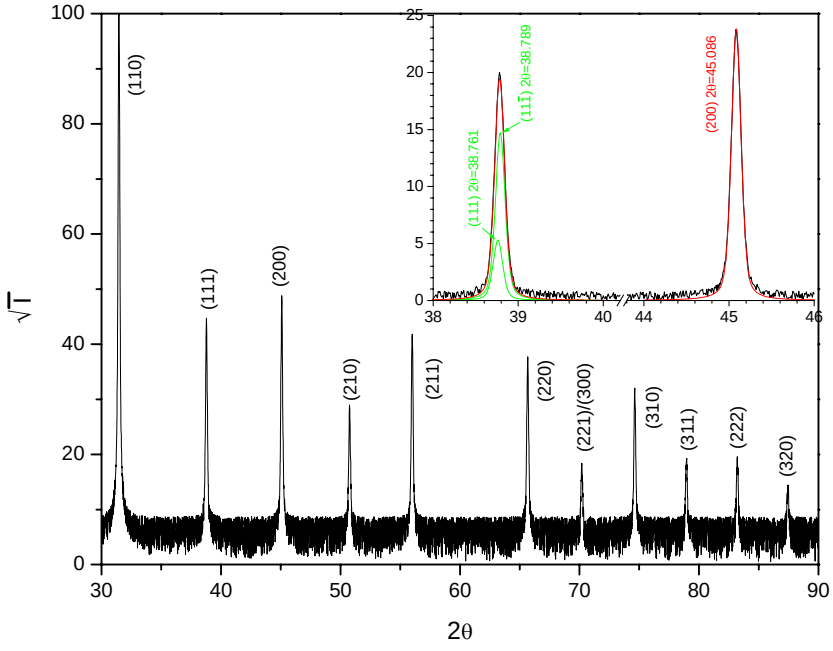

Figure 22: X-ray diffraction spectrum for 8%Zr:$BaTiO_3$. The insert shows the fitting for the (111) and (200) peaks, matching a rhombohedral phase.

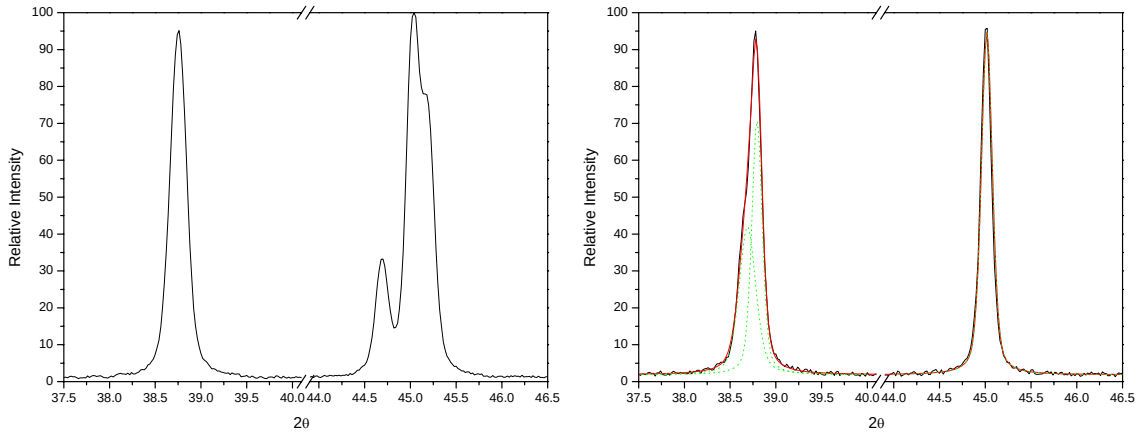

Figure 23: X-ray diffraction spectrum of 10%Hf:$BaTiO_3$ showing both the tetragonal and rhombohedral splitting prior to poling (left), compared to only rhombohedral split after poling (right).

2.2. Electron Microscopy and Chemical Analysis

The second sintering stage was not sufficient to achieve homogeneous, high density materials. Zr-doped $BaTiO_3$ showed variations of 1-2% in composition. Chemical analysis of an 8%Zr-doped material showed large grains (8-10μm) with 7% Zr and smaller grains (2-4μm) with 9.4% Zr. The inter-grain phase showed variations in composition, with values of 7-9% Zr. Since the size of the grain boundaries is actually smaller than the interaction region of the electron beam with the sample, these variations are probably the results of variations in neighboring grains.

The Hf-doped $BaTiO_3$ showed a higher level of inhomogeneity, with a second phase of $BaHfO_3$ showing in the X-ray pattern after the first and second sintering stages (see Figure 25). Electron microscopy confirms this second phase, although it is difficult to assess its composition. Average composition throughout most of the sample is the expected 11%, with the Hf-rich areas having a composition of 28%. A closer look, however, shows that the Hf-rich areas are actually a conglomerate of small Hf-rich, and Hf-poor micro-grains. Since these grains are smaller then the resolution of the micro-probe, their actual composition can not be measured.

Exaggerated growth in $BaTiO_3$ based materials is related to the formation of a liquid phase at the grain boundaries. Excess Ti has a small solubility with $BaTiO_3$, forming a

$BaTiO_3$+liquid region above 1322°C (see phase diagram in Figure 5). To prevent exaggerated grain growth, pure $BaTiO_3$ is usually sintered below 1300°C. The addition of refractory elements, such as Zr and Hf require an increase in sintering temperature. To prevent grain boundary liquid formation, powders are mixed with a small (less then .1%) deficiency in Ti. The Hf-rich areas of the sample, serve as nucleation centers for the exaggerated growth, with 60μm grains showing after 2-3 hours at 1200°C. This suggests that a ternary eutectic might exist for the BaO-HfO_2-TiO_2 system, having a lower melting point then the binary eutectic. Previous reports on Sn and Zr additions to $BaTiO_3$ support such behavior [38].

The density of the sample even after the second sintering stage is very low, as is obvious from the large number of pores seen in Figure 24. An additional sintering stage was performed to improve homogeneity. Following this third sintering stage, the relative density reached about 97.5% of theoretical density as summarized in Table 5. The same composition as Figure 24 is shown in Figure 26 following the third stage of sintering. Back scattered electron show homogeneous grains.

Figure 27 shows $BaTiO_3$ with 8% Zr after three sintering stages. The grains appear facetted with an inter-grain phase apparent, especially at triple points. Some triple points showed pores, indicating that densification was not 100% complete. Analyzing pore distribution and size, a final density of 98-99% is estimated. Lattice parameter was calculated from the x-ray measurements (see Chapter 5:2.1, page 69) and the theoretical density (ρ_{th}) was calculated using:

$$\rho_{th} = \frac{M.W.}{V_{uc} N_A} \qquad (30)$$

M.W. is the molecular weight, V_{uc} is the unit cell volume, and N_A is Avogadro's number.

For 8%Zr in $BaTiO_3$ the density is 6.058 g/cm^3. Samples were weighed and their physical dimensions were measured in order to calculate the density. For 8%Zr:$BaTiO_3$ a density of 5.905 g/cm^3 was measured, corresponding to 97.5% of the theoretical density. Similar results for other Zr- and Hf- doped $BaTiO_3$ were obtained, and are listed in Table 5.

Table 5: Density calculations from X-ray and from weight measurements.

Material	Lattice Parameter [Å]	$\rho_{x\text{-}ray}$ [g/cm^3]	ρ_{weight} [g/cm^3]	Relative density
7%Zr	4.017	6.054	5.89	97.3%
8%Zr	4.0185	6.058	5.905	97.5%
10%Zr	4.023	6.060	5.91	97.5%
15%Zr	4.031	6.079	5.92	97.4%
8%Hf	4.0215	6.223	6.075	97.6%
10%Hf	4.025	6.274	6.11	97.4%
11%Hf	4.027	6.297	6.14	97.5%
15%Hf	4.0335	6.399	6.22	97.2%

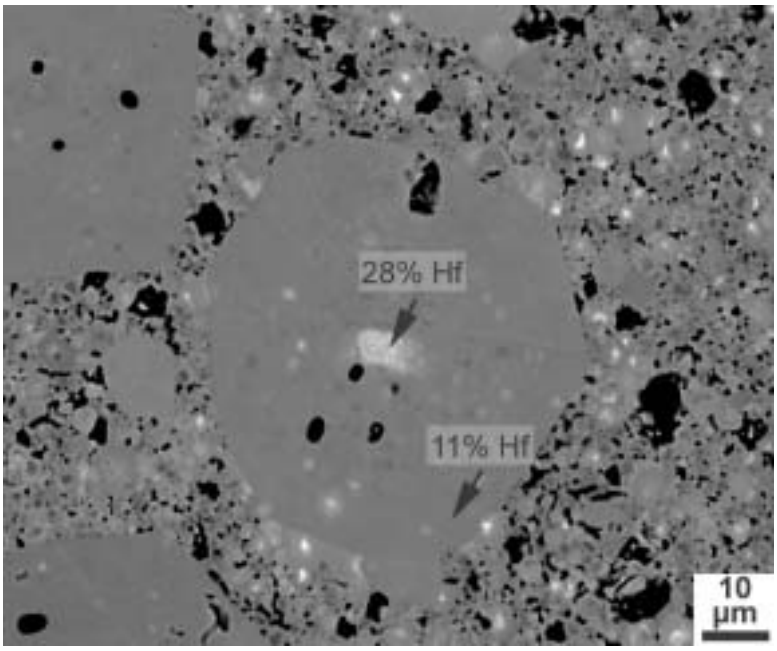

Figure 24: Backscattered electron image of $BaTiO_3$:11%Hf after the first sintering.

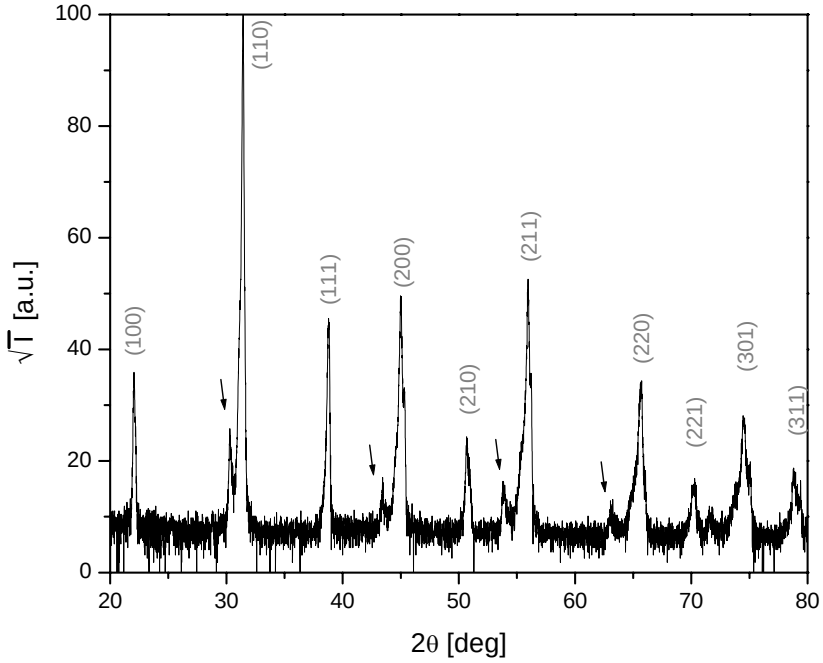

Figure 25: X-ray diffraction spectrum of $BaTiO_3$:11%Hf after the first sintering. The arrows point to a minority phase, $BaHfO_3$.

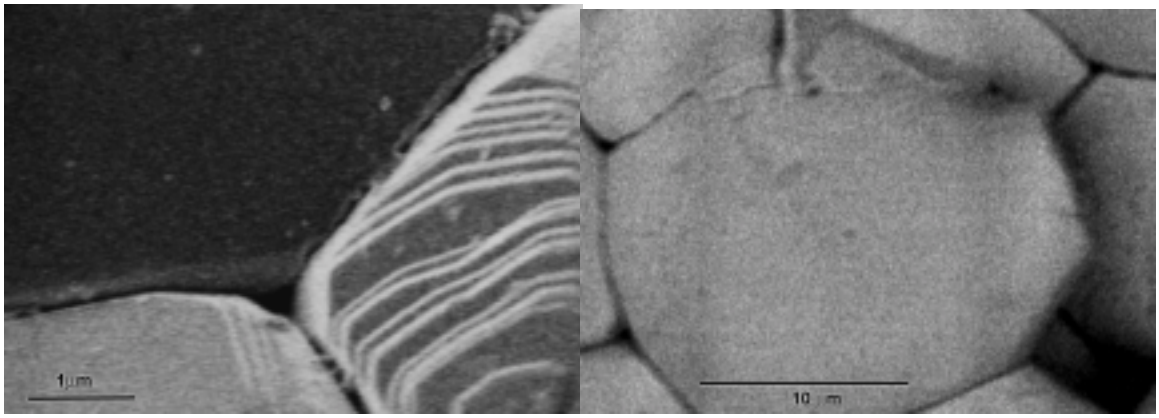

Figure 26: $BaTiO_3$:11%Hf after the third sintering stage, showing secondary electrons image (left) and backscattered electrons image (right).

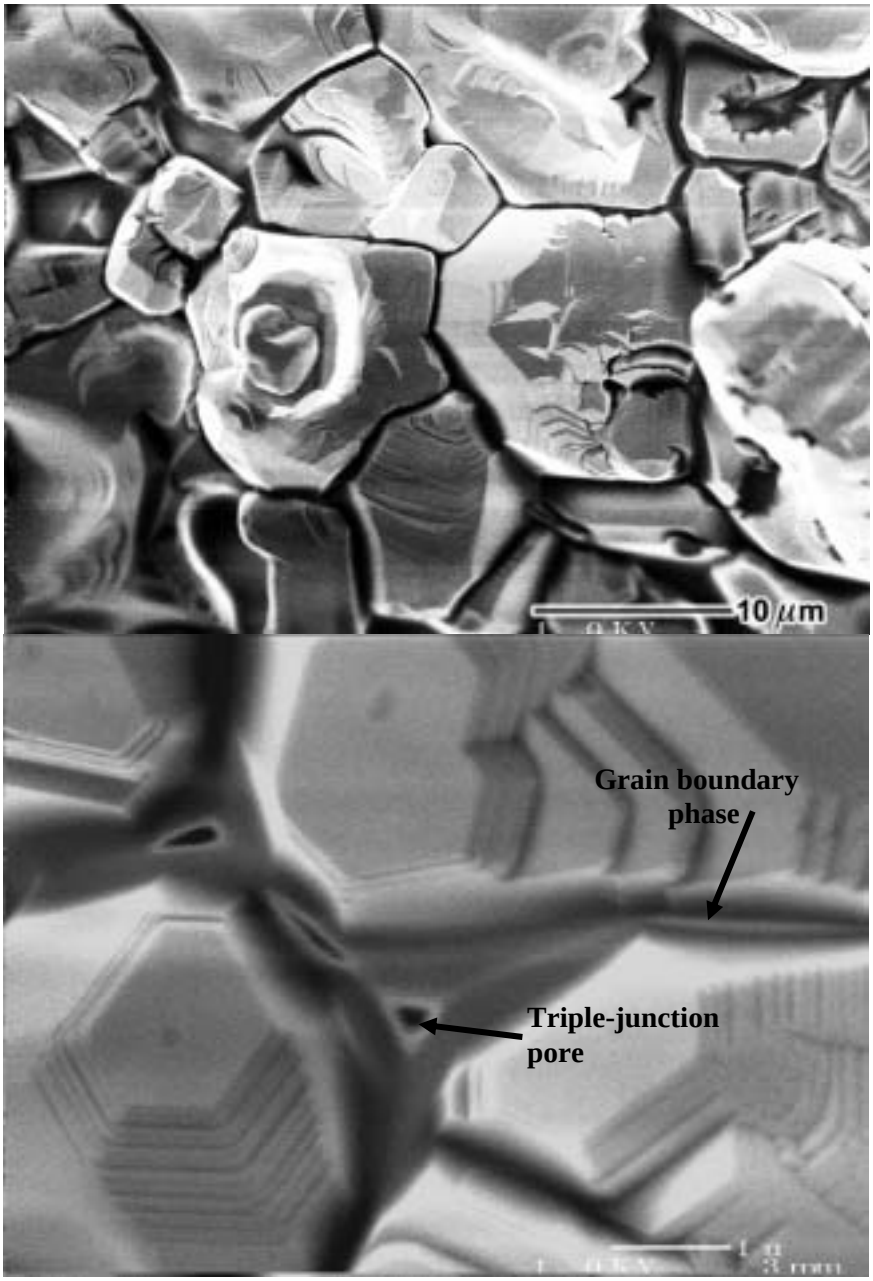

Figure 27: SEM pictures of $BaTiO_3$ with 8%Zr. The top image, taken at a lower magnification, shows the high density of the material. The bottom image shows a close-up on pores at triple-junctions.

2.3. Dielectric Properties

Dielectric measurements were performed using a Solatron impedance analyzer. Given the high impedance of the samples reasonable data were obtained only at the higher frequencies, as can be seen in Figure 28 for 11%Hf:$BaTiO_3$. The noisy data obtained below 10kHz make it difficult to simulate an appropriate equivalent circuit. The impedance of a circuit simulated for the high frequency range is shown in Figure 28. The high impedance at lower frequencies could be attributed to the high resistivity of the sample ($\rho>10^8$ Ω-cm). In order to lower the impedance, a 10MΩ resistor was connected in parallel to the sample. The improvement in the measured spectra can be seen in Figure 29. The equivalent circuit in Figure 29 shows that the sample can be considered as a pure capacitor, with:

$$Z'' = -\frac{1}{\omega C} \tag{31}$$

It is therefore possible to use a single frequency measurement in order to find the dielectric constant with little error. For the $BaTiO_3$:11%Hf sample, the equivalent circuit gave a capacity of C=9.88±0.02 pF, while the value measured at 10kHz was C=9.90 pF.

Samples of several compositions were put in a furnace and connected to an HP4192 impedance analyzer. Dielectric constant measurements were performed at a frequency of 10kHz, to ensure that the impedance was not too high. The dielectric constant as a function of temperature for 10% and 15% Hf doped $BaTiO_3$ is shown in Figure 30. The dielectric constant as a function of temperature for Zr-doped $BaTiO_3$ is shown in Figure 31.

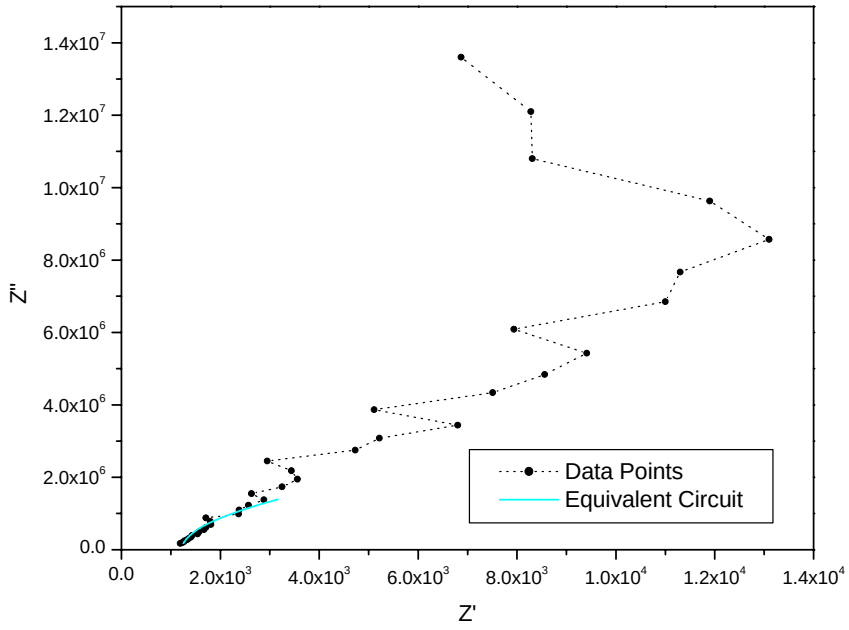

Figure 28: Impedance plot for 11%Hf:$BaTiO_3$. Below 10 kHz the impedance is too high, resulting in inaccurate measurements. Note that the Z" scale is three orders of magnitude larger then the Z' scale.

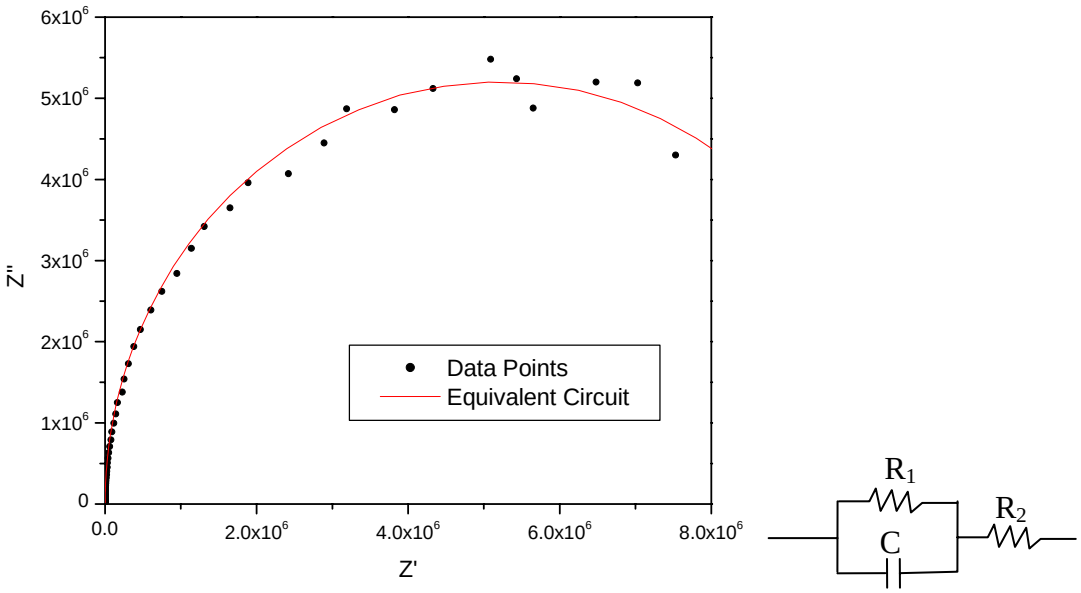

Figure 29: Impedance plot for 11%Hf:$BaTiO_3$ with a 10MΩ resistor in parallel. The equivalent circuit is R_1=10±.05 MΩ, R_2=1.5±0.1 kΩ, and C=9.88±0.02 pF.

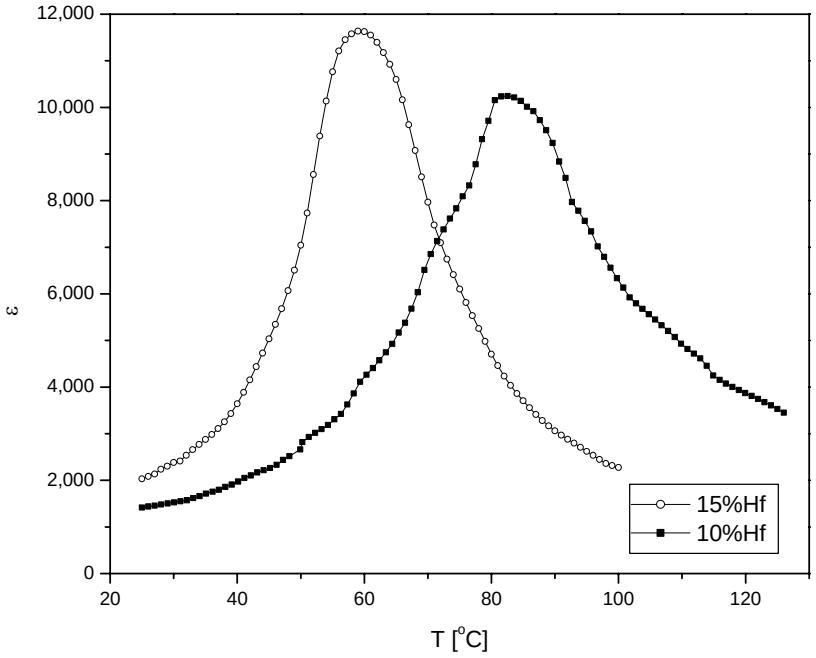

Figure 30: Dielectric measurements for $BaTiO_3$ with 10% and 15% Hf. as a function of temperature.

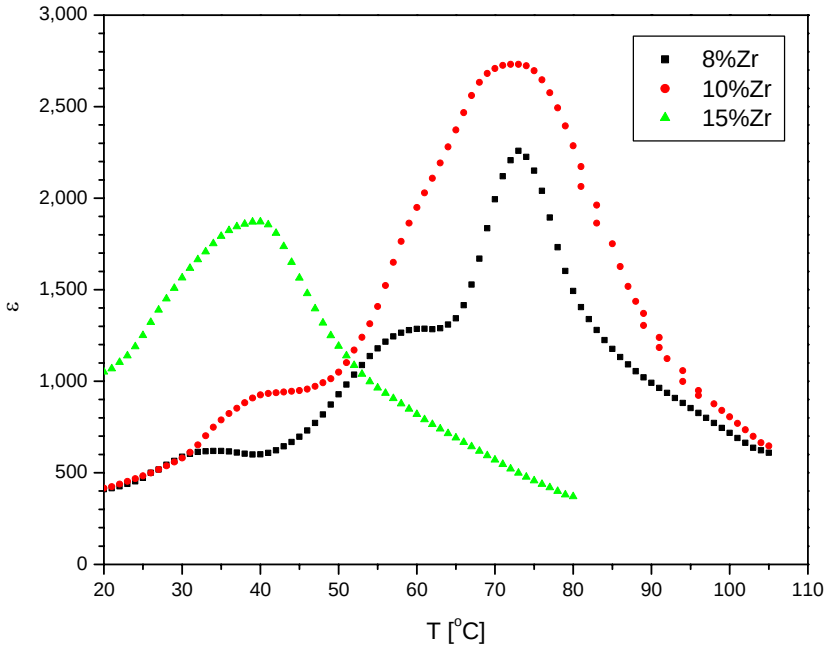

Figure 31: Dielectric constant as a function of temperature for Zr doped $BaTiO_3$.

2.4. Electromechanical Testing

The polarization hysteresis loop was calculated by integrating the current during the piezoelectric testing. Figure 32a shows the results for $BaTiO_3$ with 7%Zr. The hysteresis loop is very narrow, with a coercive field around 2-3 kV/cm. The samples doped with $KNbO_3$ showed an almost paraelectric response as can be seen in Figure 32b.

The piezoelectric response was measured for the different samples and compared to that of standard PZT samples. A sample of pure $BaTiO_3$ was also prepared for comparison. Figure 33 shows the strain vs. field response for different materials. It can be seen that all the rhombohedral phase-stabilized $BaTiO_3$ samples show a significant improvement over the pure (tetragonal) phase.

Samples were tested after subsequent annealing. The effect of chemical inhomogeneity (see Chapter 4:2.2, page 14) are also evident in the piezoelectric response. Figure 35 shows the response of a sample after the first sintering stage compared to that of a sample measured following the second sintering stage. For a complete list of the piezoelectric properties, see

Table 7 on page 78.

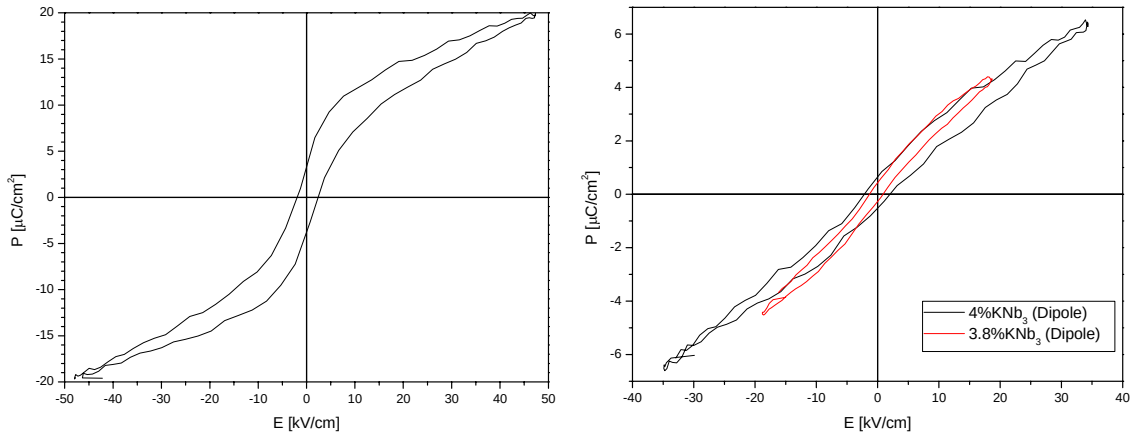

Figure 32: Polarization hysteresis loops for $BaTiO_3$ with 7%Zr 3.8% $KNbO_3$ and 4%$KNbO_3$.

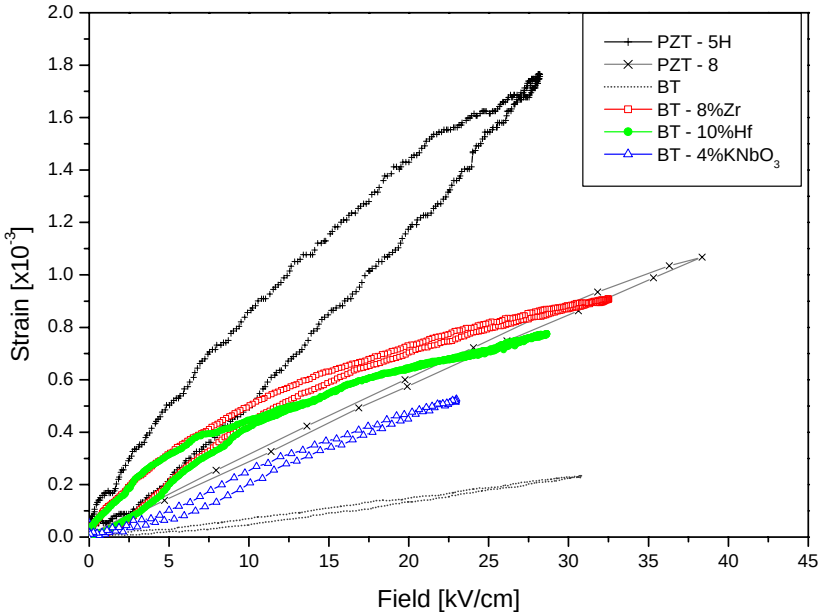

Figure 33: Strain vs. electric field behavior of doped $BaTiO_3$ (4%$KNbO_3$, 8%Zr, 10%Hf) compared to standard PZT and pure $BaTiO_3$.

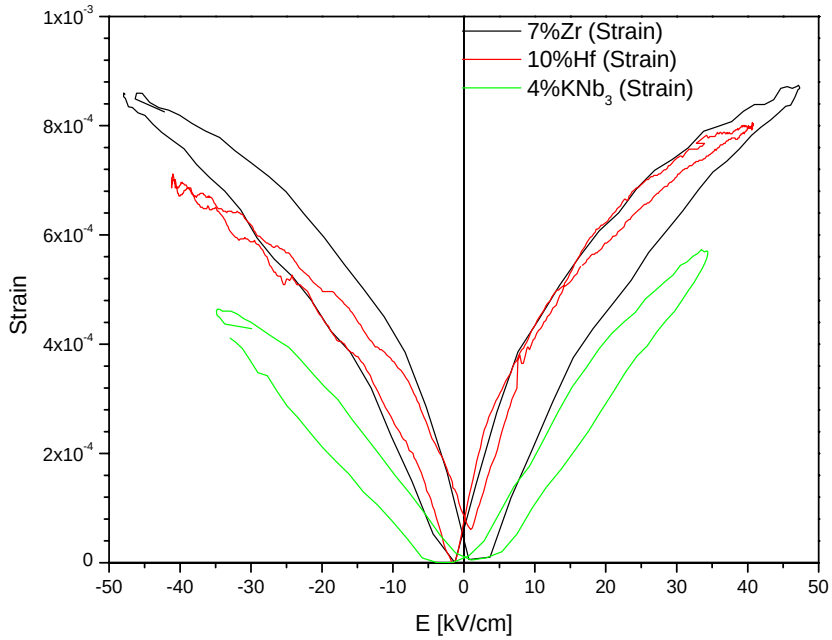

Figure 34: Strain vs. electric field hysteresis loop for doped $BaTiO_3$ (4%$KNbO_3$, 7%Zr, 10%Hf).

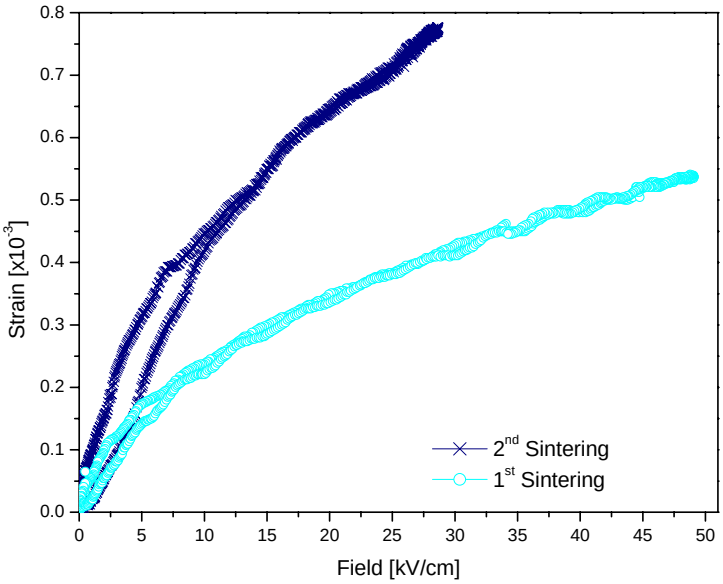

Figure 35: Piezoelectric response for $BaTiO_3$:11%Hf. The light circles represent a sample after the first sintering stage and the dark X's after the second sintering stage.

3. Thin Films

3.1. Thickness and Roughness

A characteristic profilometry measurement of a $BaTiO_3$ film grown on MgO is shown in Figure 36. Ellipsometry measurements for this sample gave a thickness of 520-540nm, compared with the 470-530nm from the profilometer. The thickness variations are not due to roughness, but rather a gradient of 15% over the entire substrate (1x1cm^2). This is an intrinsic problem with our PLD system, since one can not rotate or move the substrate during deposition. AFM measurements were performed on several samples; however, such scans took longer to run and do not add much information. Roughness was, therefore, assessed using the profilometry scans.

Thickness measurements were used to evaluate the deposition rate. Deposition rate as a function of substrate temperature and laser fluency is shown in Figure 37. Substrate temperature plays a very small role in deposition rate, with a change of less then 10% over the entire range examined. Deposition rate goes up with fluency up to 3 J/cm^2, at

which point it saturates at around 0.33Å/pulse. Changing the deposition frequency does not affect the deposition rate per pulse. The result is a deposition rate of 10nm/min at 5Hz, and around 60nm/min at 30Hz. Figure 37 also shows a pure $BaTiO_3$ film compared with a Zr doped one, both deposited under the same conditions. Both the deposition rate and the gradient throughout the sample are the same, suggesting that doping has little effect on the deposition mechanism, in particular on the ablation rate and the angular distribution of the plume.

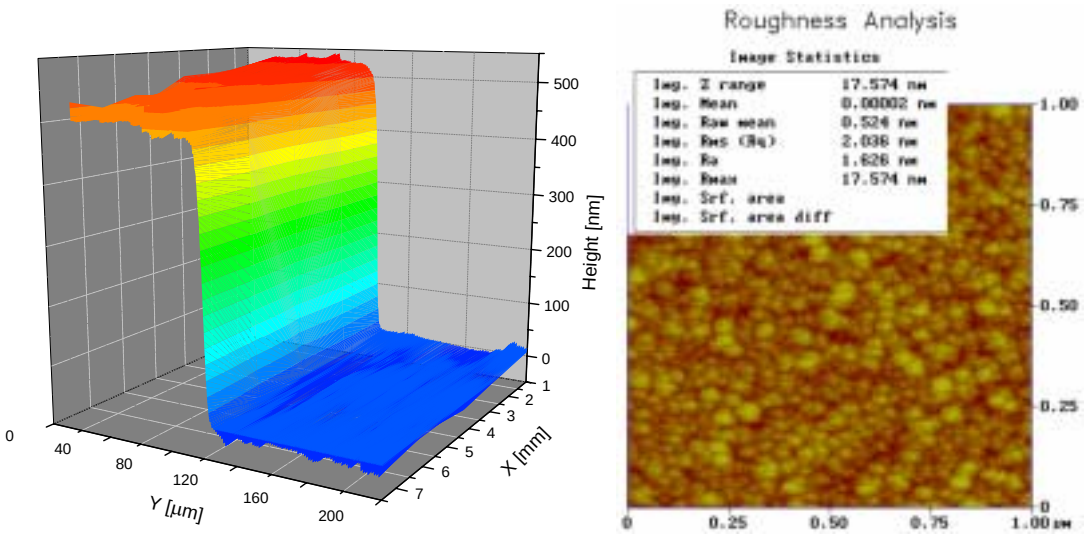

Figure 36: Profilometry measurements for $BaTiO_3$ film grown on MgO (left) and an AFM scan (right).

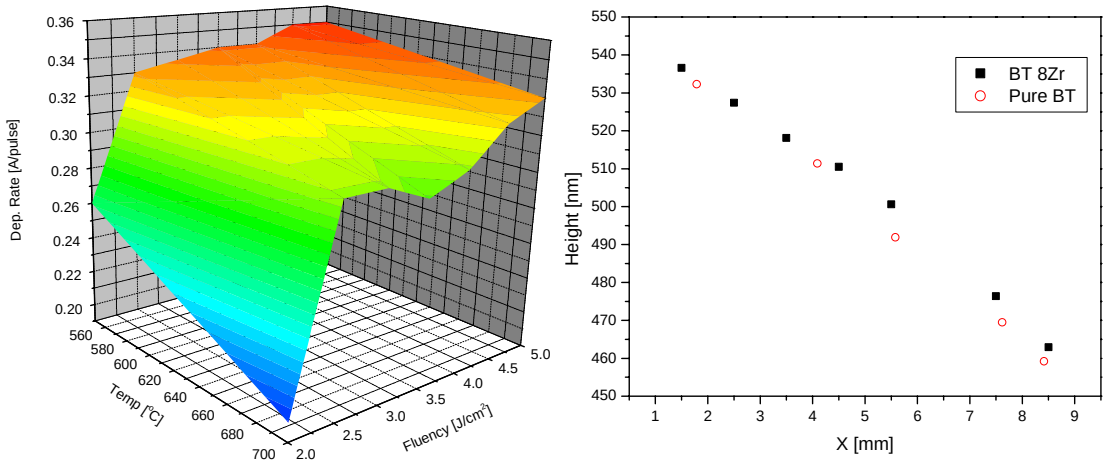

Figure 37: Deposition rate as a function of substrate temperature and laser fluency (left), and a comparison of pure and Zr-doped $BaTiO_3$ deposition (right).

3.2. X-ray

General

X-ray data for $BaTiO_3$-based films is presented in this section. Since there is a lattice mismatch between the substrate and the film, most of the films grow strained. In the following sections strain is calculated compared to bulk material having the same composition. For calculations of the bulk lattice parameter see Chapter 5:2.1.

Growth on MgO

Samples were aligned for X-ray diffraction using the MgO (200) peak for MgO substrates and Si (400) for SOI substrates. Figure 38 shows the diffraction pattern for $BaTiO_3$:8%Zr grown at 650°C and 700°C. At 650°C, the (111) and (002) peaks are visible, matching a 2.2% strained $BaTiO_3$. At 700°C, the (110) and (002) peaks are visible, matching a 1.6% strain. Growth at 700°C and a higher fluency shows (200)/(002) peaks with a strain of 0.6%. The high resolution diffraction pattern in Figure 39 is characteristic of samples grown at low temperature. The $BaTiO_3$ peak is sharp in the θ–2θ direction ($\Delta\theta$ axis), indicating good crystallinity. In the ω direction, however, the peak is very wide, indicating a low level of orientation.

At higher temperature, films with higher levels of orientations were obtained. An example of $BaTiO_3$:10%Hf grown at 700°C is shown in Figure 40. The film shows only the <110> family of peaks in standard diffraction. High resolution diffraction confirms the orientation, with a very narrow peak in ω space.

A summary of strain and orientation for films grown at different substrate temperature is shown in Figure 41.

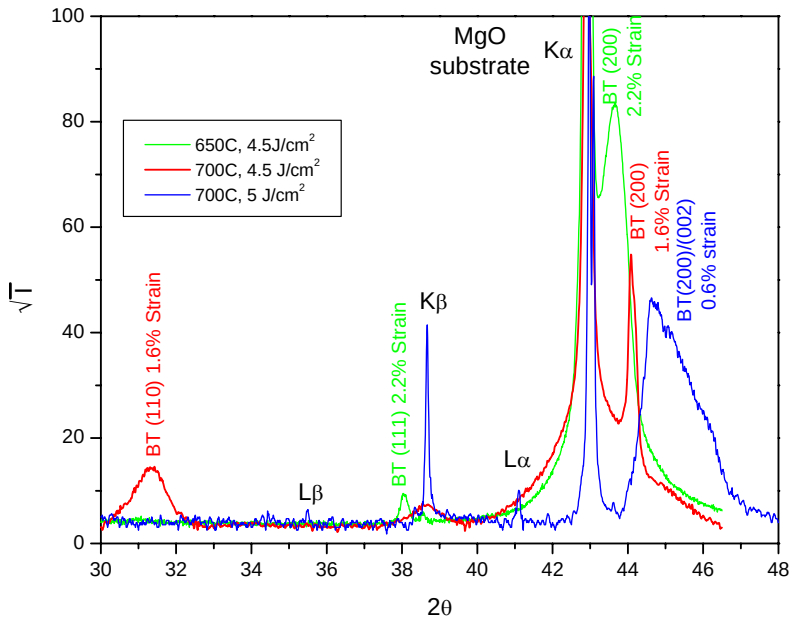

Figure 38: X-ray diffraction spectrum for $BaTiO_3$:8%Zr on MgO, showing the change in strain and orientation as a function of temperature and fluency.

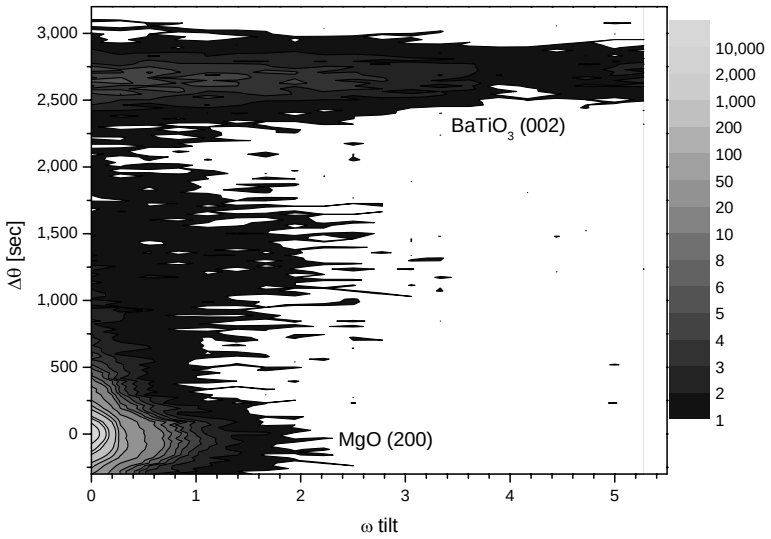

Figure 39: A high resolution scan around the MgO(200) peak for a sample grown at 600°C shows a wide ω-stability for the $BaTiO_3$ peak, indicating low level of orientation.

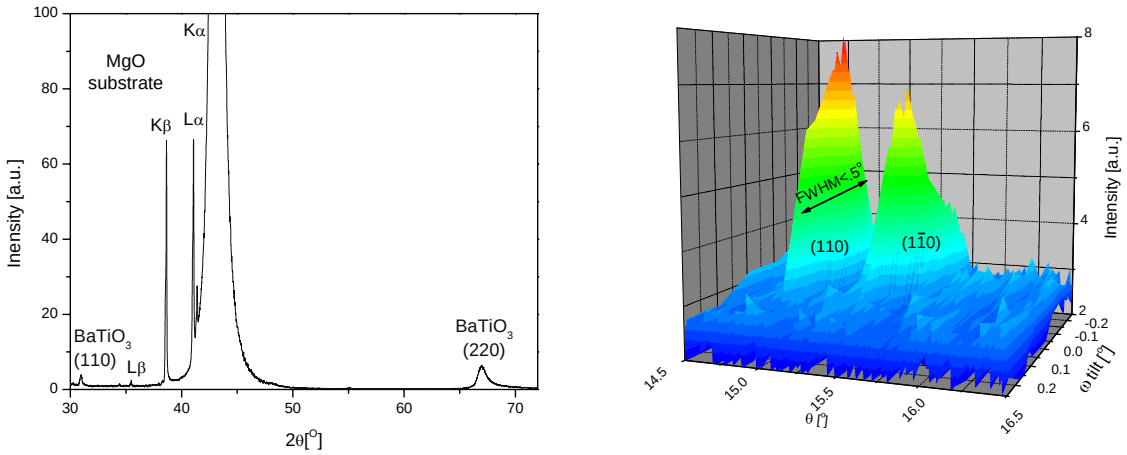

Figure 40: X-ray diffraction spectrum of $BaTiO_3$:10%Hf. Only (110) peaks are visible in the diffraction pattern (left), and a high resolution scan showing a high degree of orientation, indicated by narrow ω peaks.

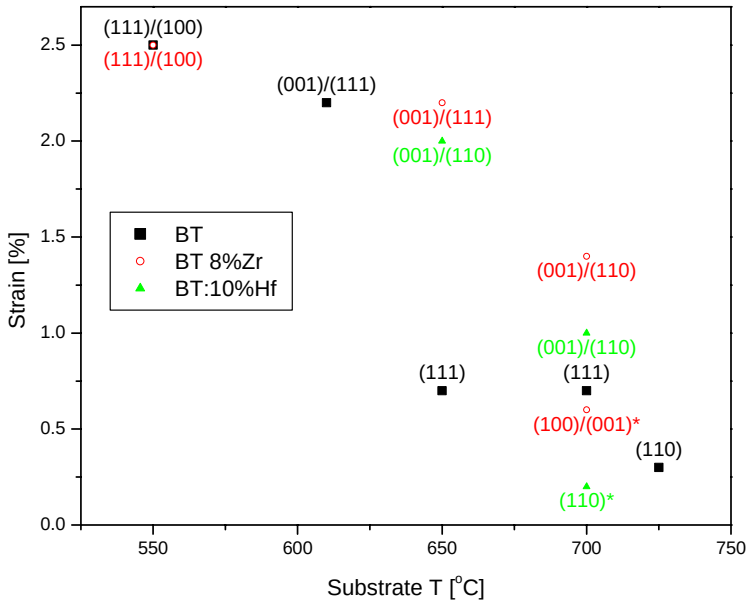

Figure 41: Summary of film orientation and strain as a function of substrate temperature. Films were grown using fluency of 3.5-4 J/cm^2, with the exception of the two samples marked with '*', that were grown using 5 J/cm^2.

Growth on SOI

Growing $BaTiO_3$ directly on SOI results in an un-oriented film, even when done at elevated temperatures. X-ray diffraction of one such film is shown in Figure 42. The MgO is oriented in the (100) direction, however the diffraction peak is very broad. The $BaTiO_3$ is mostly (111) oriented, but longer scans reveal traces of (211) peaks.

Details of the growth and characterization of MgO are given in Appendix A:.

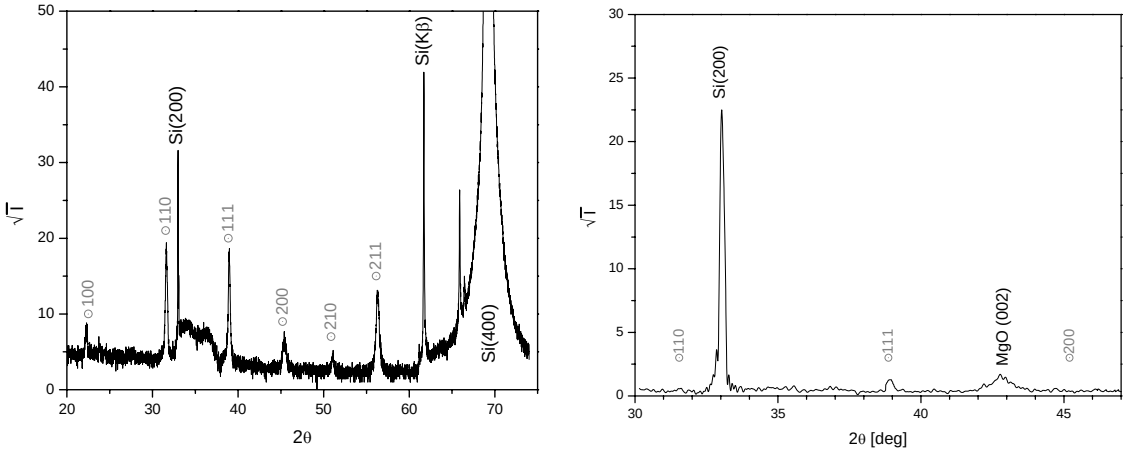

Figure 42: X-ray diffraction for $BaTiO_3$ grown on SOI at 700°C (left), and $BaTiO_3$ on MgO on SOI (right).

3.3. Optical Properties

The refractive index is plotted in Figure 43 as a function of substrate temperature and film composition. Films grown at a temperature lower then 550°C had very low refractive indices, indicative of amorphous films. The low level of crystallinity is also obvious from x-ray diffraction of these films.

Metricon measurements were performed at wavelengths of 660nm, 1380nm, and 1550nm. The average of TE and TM measurements for pure $BaTiO_3$, 8%Zr:$BaTiO_3$, and 10%Hf:$BaTiO_3$ are shown in Figure 43. As expected the index goes slightly down at longer wavelengths.

Transmission measurement as a function of wavelength for pure $BaTiO_3$ is shown in Figure 44. The film measured was 1μm thick, which resulted in interference oscillations.

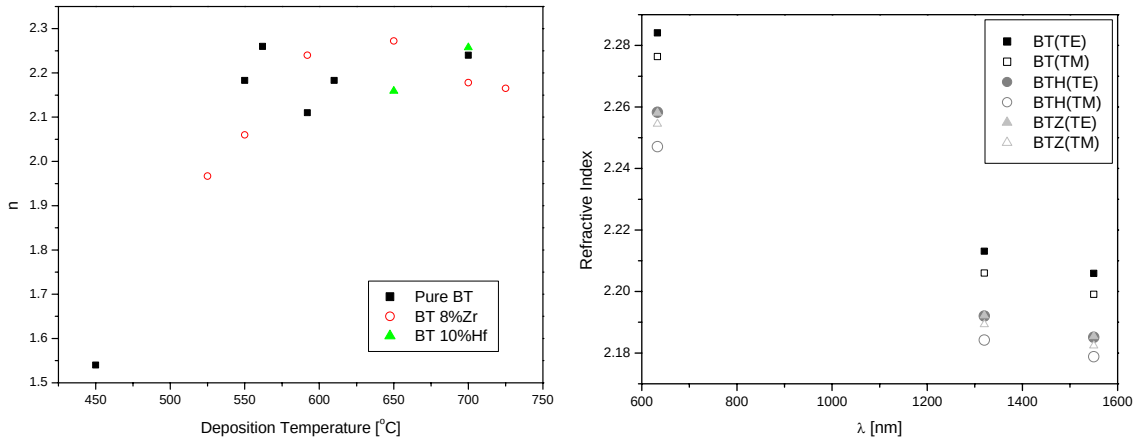

Figure 43: Index of refraction of $BaTiO_3$ based thin films: (a) Values from ellipsometry measurements as a function of substrate temperature, and (b) Metricon measurements as a function of wavelength.

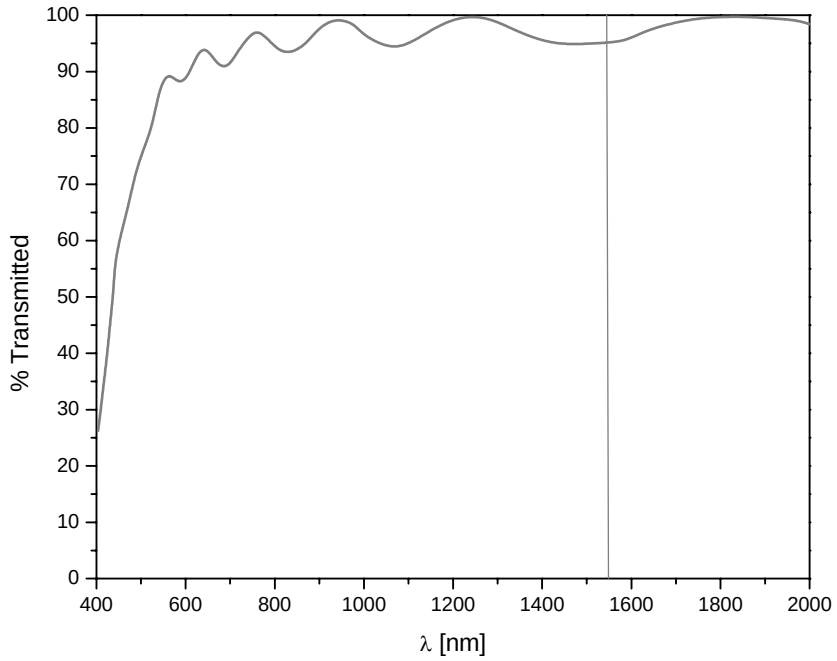

Figure 44: Transmission measurements through a 1μm thick $BaTiO_3$ film. The vertical line at 1550nm represents the region of interest in optical communications.

Samples were heat treated to evaluate the thermal stability of the index of refraction. The index as a function of temperature is plotted in Figure 45. The sample with 10% Hf shows a change of slope of the TM index around 60°C and a discontinuity around 80°C. These appear to be related to the phase transitions expected for this composition. The in-plane directions are strained by the substrate, and therefore the structural phase transition is limited to the direction perpendicular to the film. TE propagation is related to light polarized in the plane of the film, and therefore the impact of phase transitions is not observed.

After cooling back to room temperature, a small hysteresis was observed. In order to understand the source of this hysteresis, the samples were heated, held at temperature and then cooled down to room temperature. The index of refraction was measured after each such anneal, together with x-ray diffraction. The optical measurements are shown in Figure 46 for a pure $BaTiO_3$ and an 8%Zr $BaTiO_3$. For both films, the changes for the TE mode are within the error of the measurement The TM mode, however, shows a drop in the index when treated at 60°C or more. The drop is small, 2×10^{-3} for pure $BaTiO_3$ and less then 1×10^{-3} for the 8%Zr sample, and is independent of the anneal temperature. X-ray analysis of the samples after these anneals did not reveal any change to the crystal structure or strain level, although any such changes are expected to be very small and might be under the experimental resolution.

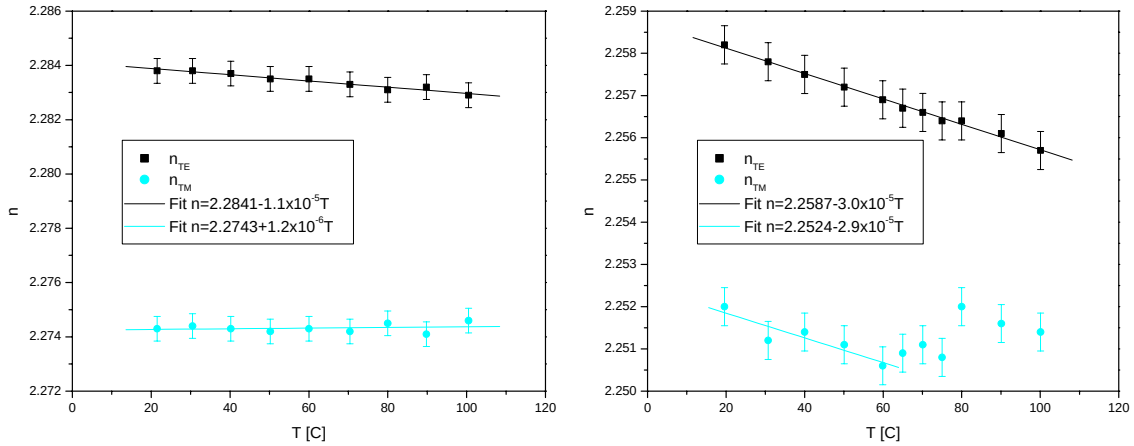

Figure 45: Index of refraction as a function of temperature for (a) $BaTiO_3$ on MgO, and (b) $BaTiO_3$:10%Hf on MgO

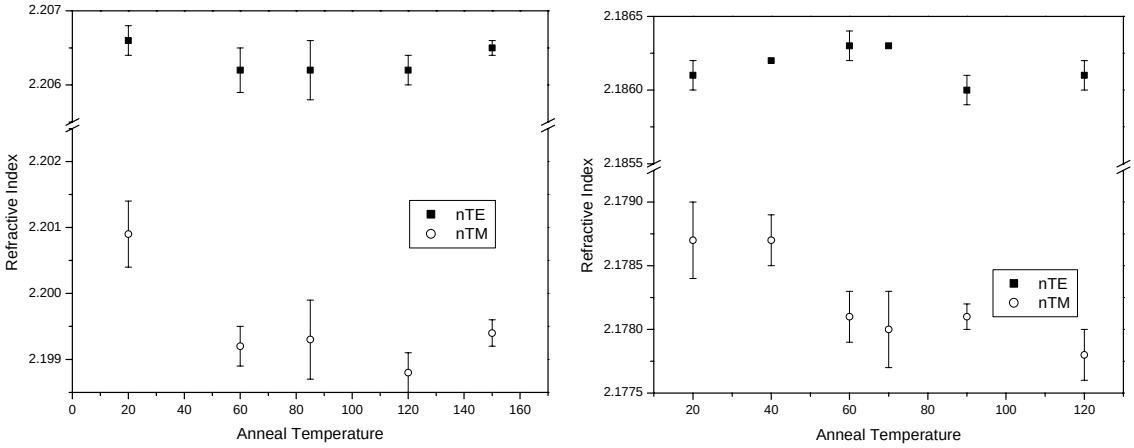

Figure 46: Refractive index of films after low temperature annealing. Pure $BaTiO_3$ (left) and $BaTiO_3$:8%Zr (right).

Chapter 5: Discussion

1. General

This section is again divided into two sections: one on bulk – followed by one on thin films. Then we end with the conclusions.

A key innovation of this thesis is related to investigation of the properties of the rhombohedral phase of $BaTiO_3$. It is therefore natural to begin with the crystal structure and phase stability analysis, first through the x-ray diffraction data, and then through the dielectric measurements. The bulk analysis is concluded with an analysis of the potential effects of second phases on the piezoelectric response.

The thin film analysis follows a similar logic, discussing film deposition conditions and their impact on the optical properties.

2. Bulk Materials

2.1. Phase Stability and Lattice Parameter

The phase diagram for Zr- and Hf- $BaTiO_3$ was shown in Figure 6. In both cases there is a pinching of the transition temperatures in the vicinity of the compositions being investigated. Such pinching indicates that the thermodynamic local minima for the different phases are energetically close. The addition of local strain can further add to the possible local minima in the energy domain, and sometimes global minima in local regions of the physical domain. This can result in meta-stable phases. In particular, since during cool-down the material goes through the tetragonal phase, that phase may remain meta-stable upon further cooling. For the higher doping levels (15%Hf, 15%Zr), the material passes directly from cubic to rhombohedral, without going through the tetragonal phase. These materials did not show any presence of the meta-stable tetragonal phase.

As mention before (Chapter 4:2.1), cooling under a poling field stabilized the rhombohedral phase. This can be explained by looking at the thermodynamic potential.

The thermodynamic potential can be written as a function of temperature and the order parameters [39],[40]:

$$\Phi(T,\eta_1,\eta_2,\eta_3) = \Phi_0(T) + \tfrac{1}{2}\alpha(T-T_c)(\eta_1^2+\eta_2^2+\eta_3^2) + \tfrac{1}{4}\beta_1(\eta_1^2+\eta_2^2+\eta_3^2) + \tfrac{1}{2}\beta_2(\eta_1^2\eta_2^2+\eta_2^2\eta_3^2+\eta_1^2\eta_3^2)+\ldots \quad (32)$$

By minimizing the energy one can find the equilibrium solutions for the order parameters. The trivial solution of $\eta_i=0$ corresponds to the cubic, paraelectric, state. Other solutions include the tetragonal phase:

$$\eta_1=\eta_2=0,\eta_3\neq 0$$
$$\eta_1=\eta_3=0,\eta_2\neq 0 \quad (33)$$
$$\eta_2=\eta_3=0,\eta_1\neq 0$$

and the rhombohedral phase:

$$\eta_1=\eta_2=\eta_3\neq 0 \quad (34)$$

Applying an electric field one should add the following to (32):

$$\Delta\Phi_E = -a(\eta_1E_1+\eta_2E_2+\eta_3E_3) \quad (35)$$

This increases the stability of non-zero order parameters, therefore poling the material. The higher number of non-zero order parameters for the rhombohedral phase results in a larger reduction of the free energy compared to the tetragonal phase. This, in turn, makes the meta-stable appearance of the tetragonal phase less favorable. Similar behavior has been previously reported for the transition between tetragonal and orthorhombic $BaTiO_3$ [41].

The x-ray data was fitted to a rhombohedral unit cell with lattice parameter **a,** and angle α. The value of α was calculated first using the (111) and (222) lines [42]:

$$\cos\alpha_R = \frac{mN}{l(h+k)-m\cdot h\cdot k} \quad (36)$$

with:

$$m = \frac{\sin\theta_{hk\bar{l}} - \sin\theta_{hkl}}{\sin\theta_{hk\bar{l}} + \sin\theta_{hkl}}; N = h^2 + k^2 + l^2 \qquad (37)$$

Since m depends on the difference between θ_{hkl} and $\theta_{hk\text{-}l}$, the resolution of the diffractometer determines the accuracy of measuring α. For some samples, especially at the higher doping level, no (111) or (222) peak splitting was observed and the pattern was similar to cubic (Figure 47). Since the dielectric measurements show that the material is already at the ferroelectric phase (see section Chapter 4:2.3 on page 54), this should be attributed to the resolution of the x-ray instrument, making it impossible to measure α≥89.99.

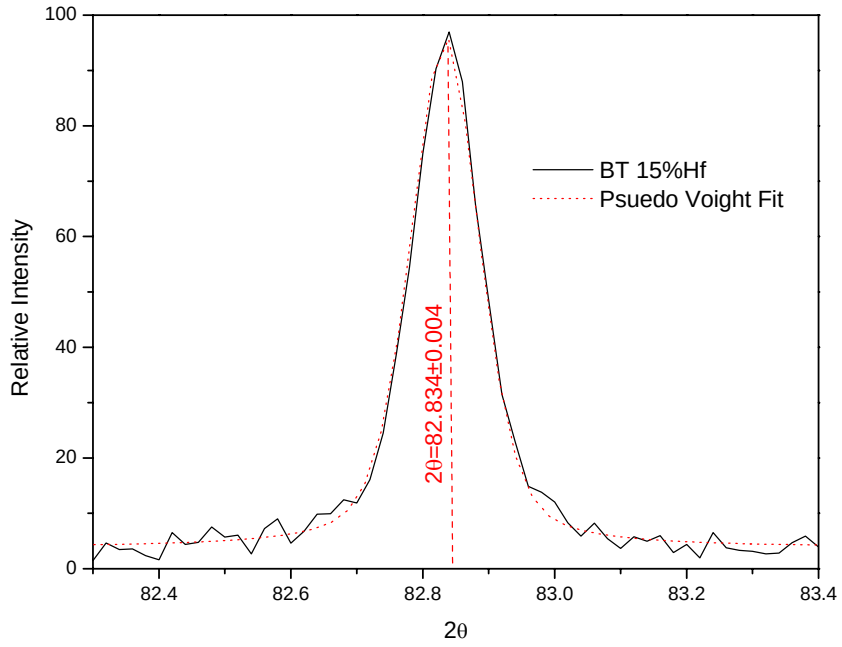

Figure 47: X-ray pattern for 15%Hf:$BaTiO_3$ showing the (222) peak. A single pseudo-Voight peak fits the curve, although the sample is rhombohedral.

Using the value of α, the lattice parameter was calculated according to:

$$a_R = \frac{\lambda\sqrt{N}}{2\sin\theta_{hkl}\left(1 + \frac{hk+kl+hl}{N}\cos\alpha_R\right)} \qquad (38)$$

The average from several (hkl) planes was taken, and is plotted in Figure 48 for both Zr and Hf solid solutions. Table 6 summarizes the lattice parameter and rhombohedral angle measured in this work.

The lattice parameter exhibited a linear dependence on the doping percentage of Zr and Hf, as illustrated in Figure 48. Using the molar fraction [Zr] and [Hf], the following fits were obtained for the rhombohedral lattice parameter:

$$a = 4.005 + (0.18 \pm 0.005) \cdot [Zr] \text{ Å} \quad (39)$$

$$a = 4.008 + (0.17 \pm 0.005) \cdot [Hf] \text{ Å} \quad (40)$$

In both cases the rhombohedral distortion was very small, with 89.95°<α<90°. It is interesting to note that the volumetric lattice parameter ($\sqrt[3]{a^2 c}$) for pure $BaTiO_3$ at room temperature is 4.006Å - 4.007Å [15], compared to ($4.005 \pm 5 \times 10^{-4}$)Å and ($4.008 \pm 5 \times 10^{-4}$)Å in equations (39) and (40).

Table 6: Summary of lattice parameter and rhombohedral angle for samples studied in this work.

	7% Zr	8% Zr	10% Zr	15% Zr	8% Hf	10% Hf	11% Hf	15% Hf	3.8% KN	4% KN
d [Å]	4.017	4.0185	4.023	4.031	4.0215	4.025	4.027	4.0335	4.009	4.006
α	89.95	89.97	≥89.99	≥89.99	89.965	89.98	89.985	≥89.99	≥89.99	≥89.99

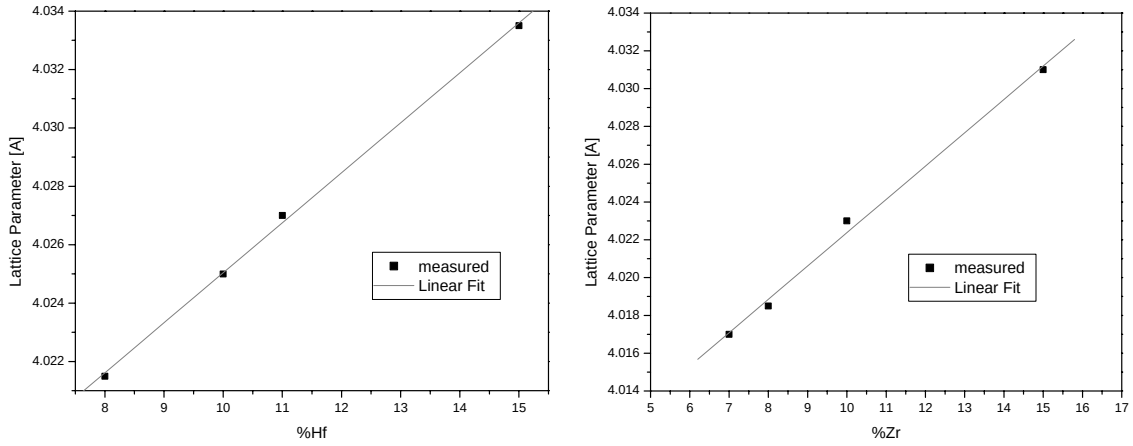

Figure 48: Lattice parameter as a function of Hf concentration (left) and Zr concentration (right) as determined from x-ray diffraction.

2.2. Dielectric measurements and phase transitions

The dielectric constant measurements, as shown in Figure 30 and Figure 31, show a distinct Curie transition. Subsequent transitions, however, are less obvious. The derivative of the dielectric constant (ε') was taken in order to find these phase transitions. The phase transitions can be seen in Figure 49 for Hf-doped and in Figure 50 for Zr-doped $BaTiO_3$. The transition temperatures extracted from Figure 49 and Figure 50 are compared to literature values in Figure 51 and Figure 52. The error in estimating the transition temperature from ε' is relatively small, ±1° for the Curie point and ±2.5° for the other transitions. This, however, is only the measurable part of the error. Samples were heated at a rate of 1-2°C/min to ensure as much thermal equilibrium as possible. Even so, small fluctuations occurred, as can be seen from the noise in Figure 49 and Figure 50. In addition, having the thermocouple in contact with the sample introduced errors in the impedance measurement. The thermocouple was, therefore, not in contact with the sample, introducing another source of error. Over all, the error in temperature reading is estimated at no more ±3°C,

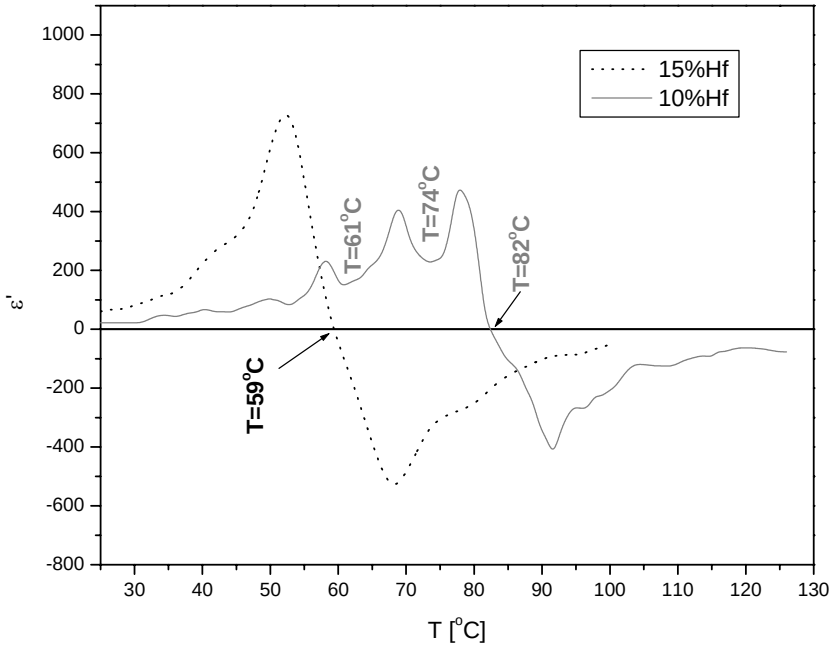

Figure 49: First derivative of the dielectric constant for $BaTiO_3$ with 10% and 15% Hf. Phase transitions are labeled with the transition temperature.

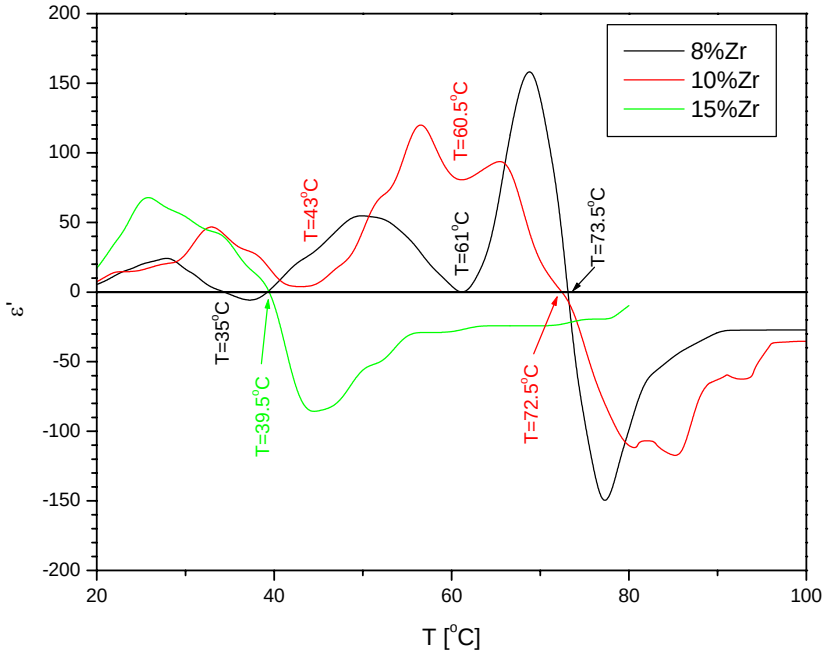

Figure 50: First derivative of the dielectric constant for $BaTiO_3$ with 8%, 10% and 15% Zr. Phase transitions are labeled with the transition temperature.

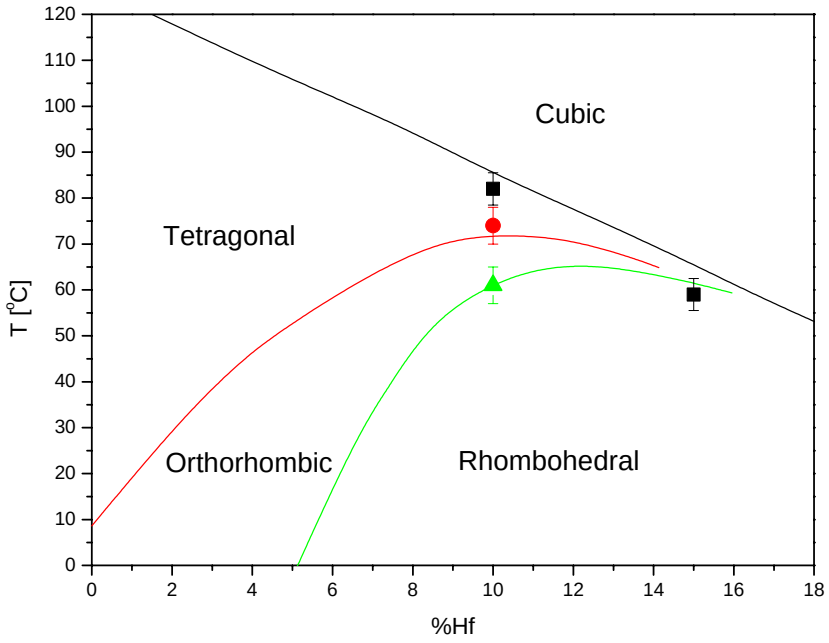

Figure 51: Phase diagrams for $BaTiO_3$:$BaHfO_3$ [16] overlaid with the measured transition temperatures.

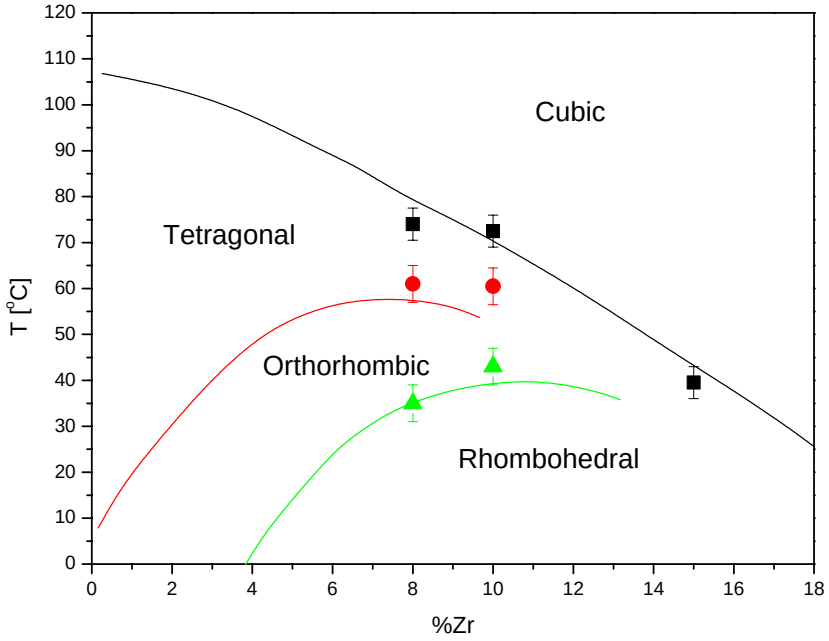

Figure 52: Phase diagrams for $BaTiO_3$:$BaZrO_3$ [17] overlaid with the measured transition temperatures.

2.3. Piezoelectric Properties

All the doped samples showed a two stage piezoelectric response, with the boundary around 12 kV/cm. For Zr and Hf doping, the low field regime is dominated by a high piezoelectric response (d_{33}>300pC/N), and the high field regime by a saturation level with d_{33}<100pC/N. The high field value is characteristic of pure $BaTiO_3$, suggesting that the material undergoes a phase transition into the tetragonal phase. As was mentioned earlier, the pinching of the phase stability regions can result in a meta-stable tetragonal phase at room temperature (see results section 2.1, and discussion section 2.1). This meta-stable phase suggests that the rhombohedral and tetragonal phases have similar free energy states, allowing for a field induced phase transition. A field induced phase transition is usually accompanied by a sharp increase in strain. Such a step is not observed in Figure 33, but rather a more continuous increase. This suggests that sample inhomogeneity may be playing a significant role in the electro-mechanical response. For a sample with a range of compositions, each composition will have a different field required for inducing a transition, resulting in a smoothing effect on the strain vs. field behavior.

The low hysteresis observed in the dielectric measurements of $KNbO_3$ doped $BaTiO_3$ (see Figure 32) is also reflected in the piezoelectric measurement. For low field the sample was fitted to a second order polynomial. The response is mostly electrostrictive, with $Q_{11}=(0.37\pm0.3)m^4/C^2$ or $M_{11}=(1.7\pm0.3)\times10^{-16}C^2/N^2$, with a small piezoelectric contribution, $d_{33}=(7\pm0.5)$pC/N. The electrostriction coefficient is 3.5 times higher then the value reported for pure $BaTiO_3$, $Q_{11}=0.11m^4/C^2$ [9]. Using equation (12) for the relationship between M and Q, one can find the dielectric constant:

$$\varepsilon = \frac{M}{Q\varepsilon_0} = 2400 \qquad (41)$$

The reason for the electrostrictive behavior is not clear. Although the x-ray diffraction is indistinguishable from the cubic phase, a Curie transition is seen in the dielectric measurements. A tetragonal distortion, even a small one, will be visible in the diffraction data. It is therefore reasonable to assume that the sample is indeed rhombohedral. The small distortion, however, might not be enough to create a strong piezoelectric response.

Another option is that the dual ion replacement is responsible for the electrostriction. Both theories require more research for verification.

At the higher field regime the 4%KN:$BaTiO_3$ becomes piezoelectric, with d_{33}=215pC/N. The transition field is similar to that observed in Zr and Hf doped materials, suggesting that this is also due to a phase transition. The sample underwent a dielectric breakdown at a lower field then the other compositions, making it unclear if the high field piezoelectric constant reaches saturation as for the other compositions.

Table 7 summarizes the piezoelectric response for the different samples examined. It can be seen that the rhombohedral phase outperforms pure $BaTiO_3$, both in respect to d_{33} and maximum strain, by almost an order of magnitude. This puts $BaTiO_3$-based materials in the same ballpark of the hard PZT (PZT8).

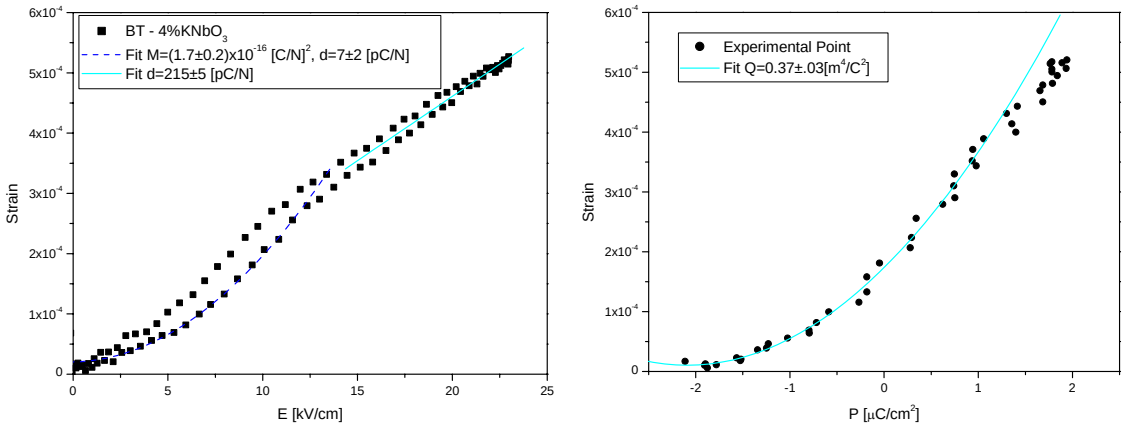

Figure 53: (a) Strain vs. electric field response of 4% $KNbO_3$:$BaTiO_3$ with a low-field electrostrictive fit and a high-field piezoelectric fit. (b) Strain vs. polarization for the same sample.

Table 7: Summary of the piezoelectric constant (d_{33}) and maximum strain (X_{max}) for the different compositions studied. In some cases a low field and high field value is given if the slope changed significantly.

	BT 7%Zr	BT 8%Zr	BT 10%Hf	BT 11%Hf	BT 4%KN	Pure BT	PZT 5H	PZT 8
d_{33} [pC/N]	450 / 75	470 / 90	450 / 80	460 / 85	7* / 215	75 (190**)	600	250
X_{max}	9×10^{-4}	1×10^{-3}	1.1×10^{-3}	8×10^{-4}	6×10^{-4}	1.5×10^{-4}	1.8×10^{-3}	1.1×10^{-3}

* This is the linear component in low field fitting of Figure 53.

** Sample measured as 75 pC/N, literature value is 190 pC/N [15].

2.4. *Effects of inhomogeneity*

The effect of inhomogeneity in the samples can be described by considering a composite material under an electric field. The dielectric mismatch between a low and a high dielectric material, results in the applied electric fields being concentrated across the defects and second phases rather then on the piezoelectric material. Simple analysis of layered structures can be found in electrostatics and electrodynamics text books [43]. A slightly more complex solution can be derived for spherical defects in an infinite matrix. The problem is shown in Figure 54. One can consider cylindrical symmetry in the φ direction, allowing for a two dimensional solution.

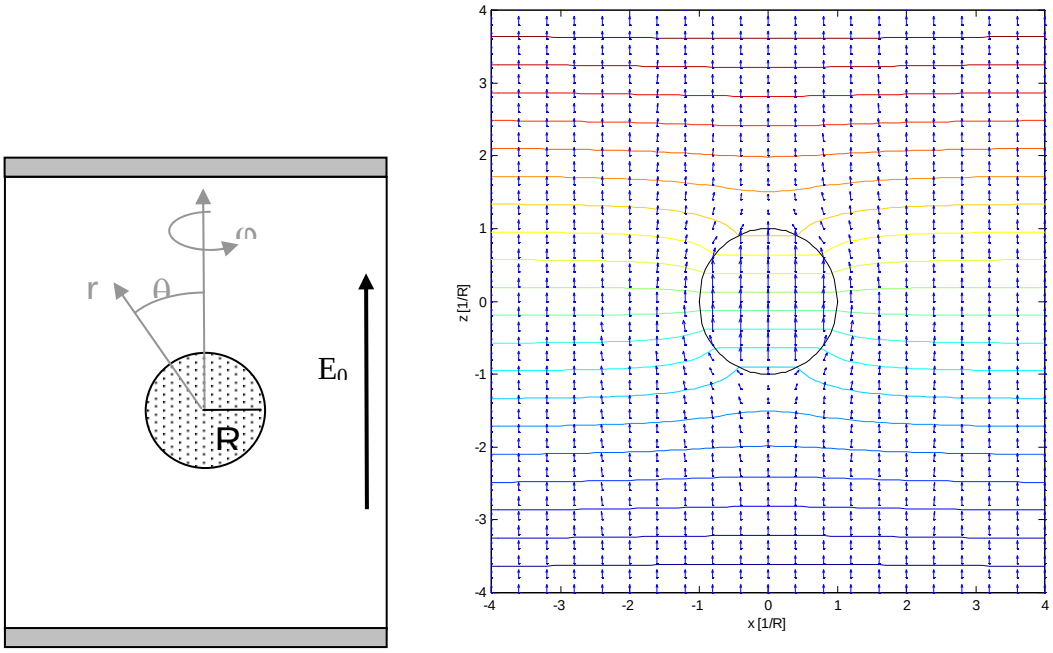

Figure 54: Spherical defect in homogeneous media: Schematic representation of the problem (left), and the solution for the potential and field distributions (right).

The solution for the electric potential in the matrix is in the form of:

$$\phi_m = \sum_{l=0}^{\infty} \left(A_l r^l + B_l r^{-(l+1)} \right) P_l(\cos\theta) \qquad (42)$$

and the solution in the defect is:

$$\phi_d = \sum_{l=0}^{\infty} C_l r^l P_l(\cos\theta) \tag{43}$$

A_i, B_i, and C_i are coefficients to be determined by boundary conditions, and P_l are Legendre polynomials. For r»R, the $1/r^2$ term can be neglected, giving $A_1=E_0$, and $A_{l\neq 1}=0$.

By taking the gradient of (42) and (43) one can write the conditions for the continuity of the displacement field at r=R gives:

$$C_1 = -E_0 + \frac{B_1}{R^3} \quad (l=1)\,; C_l = \frac{C_l}{R^{2l+1}} \quad (l\neq 1) \tag{44}$$

$$C_1 \cdot \varepsilon_d = -\left(E_0 + \frac{2B_1}{R^3}\right)\cdot \varepsilon_m \quad (l=1); C_l \cdot l \cdot \varepsilon_d = -(l+1)\frac{B_l}{R^{2l+1}} \cdot \varepsilon_m \quad (l\neq 1) \tag{45}$$

Combining (44) and (45) one finds the coefficients B and C to be:

$$B_1 = -E_0 R^3 \frac{\varepsilon_m - \varepsilon_d}{2\varepsilon_m + \varepsilon_d} \text{ and } C_1 = -E_0\left(\frac{3\varepsilon_m}{2\varepsilon_m + \varepsilon_d}\right) \tag{46}$$

$B_{l\neq 1}=0$ and $C_{l\neq 1}=0$.

The potential in the matrix is, therefore:

$$\phi_m = -E_0 r\cos\theta\left(1 + \frac{\varepsilon_m - \varepsilon_d}{2\varepsilon_m + \varepsilon_d}\left(\frac{R}{r}\right)^3\right) \tag{47}$$

which in turn give the field in the matrix as:

$$\vec{E}_m = -E_0\cos\theta\left(1 - 2\left(\frac{R}{r}\right)^3 \frac{\varepsilon_m - \varepsilon_d}{2\varepsilon_m + \varepsilon_d}\right)\hat{r} + E_0\sin\theta\left(1 + \left(\frac{R}{r}\right)^3 \frac{\varepsilon_m - \varepsilon_d}{2\varepsilon_m + \varepsilon_d}\right)\hat{\theta} \tag{48}$$

For $\varepsilon_d=\varepsilon_m$ the above term is reduced to a homogeneous field of magnitude E_0. For $\varepsilon_d \ll \varepsilon_m$ one can write the change in field from the homogeneous one as:

$$\Delta\vec{E} = \left(\frac{R}{r}\right)^3 \left(E_0\cos\theta\cdot\hat{r} + \tfrac{1}{2}E_0\sin\theta\cdot\hat{\theta}\right) \tag{49}$$

The solution for the potential and the electric field is plotted in Figure 54.

One can relate the degradation in piezoelectric and dielectric properties to the reduction in active material. Writing the effective volume fraction of active material $[A]_v$, one can use an adjustment parameter *k* to represent the zone around defects where the field is diminished:

$$[A]_V = \frac{V_{tot} - V_d(1+k)}{V_{tot}} \tag{50}$$

The $(R/r)^3$ term in (49) can be related to inverse $(1+k)$. For example, to account for the volume where the field drop is ~50% of the original value, one can use $k=1$. The sample shown in Figure 24 has about 15% voids and inclusions. This is not enough to explain the reduction of about 50% in the piezoelectric response shown in Figure 35. Going back to equation (47), one can notice that the potential is actually that of homogeneous field with an addition of a dipole at the origin. The dipole has a moment of:

$$p = -4\pi\varepsilon_0\left(\frac{\varepsilon_m - \varepsilon_d}{2\varepsilon_m + \varepsilon_d}\right)R^3 E_0 \hat{z} \tag{51}$$

This effective dipole can affect the polarization in the material. Domain formation and poling are related to long distance interaction between the dipoles in the material, and can therefore be greatly influenced by the effective dipole. A long range depoling field exerted by a defect can result in a domain forming around the defect. Since the effective dipole in the defect is always opposite to the external applied field, this domain will be of opposite polarity to the rest of the material. In a defect-free material increasing the field can sometimes cause domain reorientation, maximizing the piezoelectric effect. Since the magnitude of the defect dipole is proportional to the applied field, increasing the field will have a very limited effect. The result is twofold, first the dielectric and piezoelectric properties are diminished – both in terms of the slope an in terms of the maximum obtainable value, second the coercive field might be lowered. The coercive field is the field that is required to depole a material. This usually occurs by nucleation and growth of domains. The defect dipole can serve as a nucleation site for domains, thus lowering the coercive field.

3. Thin Films

3.1. Deposition Conditions

Laser fluency had very little influence on strain and orientation at the lower substrate temperatures. At higher temperature, however, high fluency helped reduce strain and increase the favored orientation. At higher fluency, the laser interacts more efficiently with the material cloud ablated from the target. Energy is transferred to the particles in that cloud, ionizing them into a plasma, which results in saturation of the deposition rate [44]. In addition, particles become more energetic, allowing for more surface mobility and higher levels of orientation. In Figure 41, there are two data points, for $BaTiO_3$:10%Hf and $BaTiO_3$:8%Zr, grown at 700°C and 5J/cm^2. In both cases the strain levels were reduced, and the degree of orientation increased. The particle energy can be controlled by both laser fluency and atmosphere in the chamber [45]. Lowering the chamber pressure, however, results in lower optical quality films tied to the reduction of the film.

Growth of $BaTiO_3$ directly on SOI resulted in low quality films. X-ray diffraction showed a poly-crystal structure and optical microscopy revealed surface microcracking. The lattice mismatch between $BaTiO_3$ (a~4Å) and Si (a~5.4Å) is very high, resulting in a critical thickness for dislocation formation of only several monolayers. Furthermore, the lattice mismatch for (100)BT||(100)Si is -26%, whereas the mismatch for (111)BT||(100)Si is +27%. This makes the formation of multiple orientations favorable in order to minimize stresses. The reason for the film cracking is the thermal expansion mismatch between $BaTiO_3$ and SiO_2. SiO_2 has a very low coefficient, $\alpha \sim 6\times10^{-7}K^{-1}$, while $BaTiO_3$ has a coefficient of $\alpha > 6\times10^{-6}K^{-1}$.

By growing a thin film of MgO as a buffer layer, the $BaTiO_3$ orientation becomes similar to that of films grown directly on MgO. Although the orientation is similar to growth on MgO single-crystal, the strain level in the $BaTiO_3$:MgO:SOI is high. The width of the MgO peak in Figure 42 is broader then what can be accounted for by small grain size, indicating a low crystal quality. In this case the expansion coefficient of MgO is higher

then that of $BaTiO_3$. This means that it will partly compensate for the stress introduced by the SiO_2, allowing for a higher quality $BaTiO_3$.

3.2. Refractive index

For temperatures above 550°C, there appears to be little correlation of index on temperature and composition in Figure 43. In order to try and understand this shiningly random data, a simple model was considered. The model calculates a predicted index according to the orientation and strain of the films obtained from x-ray diffraction. Since $BaTiO_3$ is birefringent, the index depends on orientation. If one has knowledge of the ordinary and extraordinary indices, one can calculate the index in any other direction (see Chapter 1:4.1). Since the indices of thin films are different from those of the bulk they were left as a fitting parameter. The relation between index and strain can be derived from the Clausius-Mossotti equation.

The Clausius-Mossotti equation relates the index of refraction (n) to unit cell volume (V) and polarizability (α) [46]:

$$\frac{\left(n^2-1\right)}{\left(n^2+2\right)}=\frac{4\pi}{3V}\alpha \qquad (52)$$

By taking the first derivative of (52) one can write the change in index as

$$\frac{\Delta n}{n}=\frac{\left(n^2-1\right)\left(n^2+2\right)}{6n^2}\left(-\frac{\Delta V}{V}+\frac{\Delta\alpha}{\alpha}\right)\approx-\frac{\left(n^2-1\right)\left(n^2+2\right)}{6n^2}\left(\varepsilon_x+\varepsilon_y+\varepsilon_z\right) \qquad (53)$$

The last approximation assumes that there is a small change in polarizability. This is easily justified when looking at strains of 10^{-3} – 10^{-2}, since the change in polarizability is on the order of 10^{-5}. The strain in the z direction was taken from the shift in X-ray peaks, while the x and y directions were calculated assuming a Poisson ratio of 0.2-0.3 [15]. These variations in Poisson ratio had very little effect on the overall results. The strain for the films was calculated using the lattice parameters measured for the bulk materials as shown in Figure 48.

The measured indices compared with results for these calculations are shown in Figure 55. The results are obtained for n_o=2.334 and n_e=2.163 as fitting parameters. Values of n=2.35-2.38 were previously reported for oriented films [47].

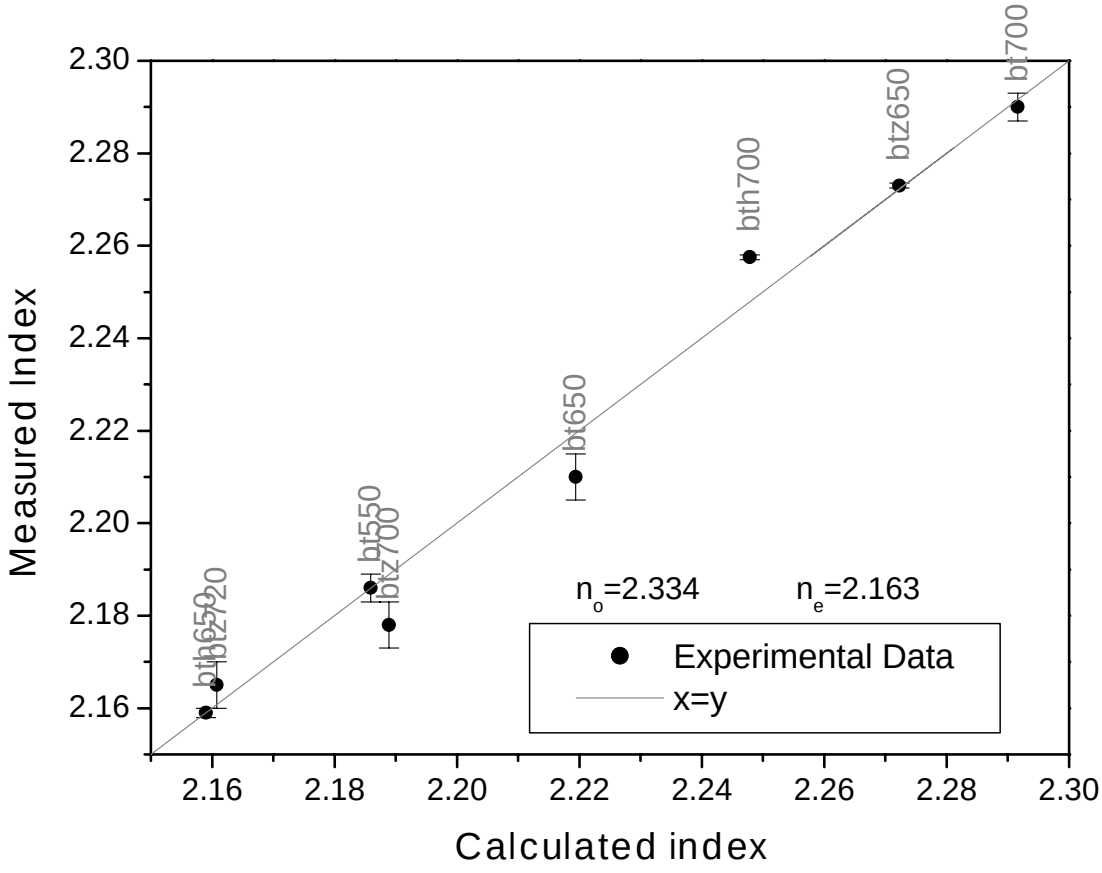

Figure 55: Measured index compared to calculated values. The films ordinary and extraordinary indices were found to be 2.334 and 2.163 respectively. Labels represent material (bt - $BaTiO_3$, btz - $BaTiO_3$:8%Zr, bth - $BaTiO_3$:10%Hf) and substrate temperature.

The simple Clausius-Mossotti calculations work very well for explaining the average index (ellipsometry measurements). Samples of different compositions were fitted using only the two indices as fitting parameters. These calculations are, however, inadequate for the polarization dependent measurements. This is of little surprise, as the equations in (52) and (53) are for isotropic materials.

3.3. Temperature Dependence of the Refractive Index

Equation (18) described the change of the optical properties due to the electro-optic effect. In practice, especially when dealing with thin films, secondary effects can come into play. In particular, strain can introduce additional changes in the optical properties. Considering the general coordinate system x_i (i=1,2,3), one can define a set of polarization constants a_{ij} so that equation (18) is re-written as:

$$a_{ij} x_i x_j = 1 \tag{54}$$

$$a_{ij} = \delta_{ij} \frac{1}{n_i^2} + p_{ijkl}^{P} X_{kl} + r_{ijk}^{x} P_k \tag{55}$$

Equations (54) and (55) use the Kroning summation notation. δ_{ij} is the Kronecker function, p^P are the piezo-optic coefficients at constant polarization, X_{kl} are the strain components, r^x are the electro-optic coefficients at constant strain, and P_k is the polarization. Assuming a diagonal initial state as represented by equation (17), the change in a can be written as:

$$\Delta a_{ij} = p_{ijkl}^{P} X_{kl} + r_{ijk}^{x} P_k \tag{56}$$

The strain can be written as a function of the stress (σ) and the polarization (P) using the compliance (s) and piezoelectric (b) coefficients respectively.

$$X_{kl} = -s_{klmn} \sigma_{mn} + b_{klm} P_m \tag{57}$$

Using equation (57) together with (56) gives an important relationship in the absence of stress:

$$\Delta a \propto (b + r) P \tag{58}$$

Since both r and b are proportional to the polarization [41], a stress free material will show a change in the refractive index that is proportional to the polarization squared. In polarized materials, the birefringence can be described using equation (58) as:

$$\Delta n = K \cdot P_s^2 \tag{59}$$

with a constant K≈1×10^8 cm^4/C^2 for $BaTiO_3$. The change of polarization with temperature is [41]:

$$\frac{dP_s}{dT} \approx 6 \cdot 10^{-8} \frac{C}{cm^2 \cdot {}^\circ C} \tag{60}$$

Using equation (59),this is correlated to a change in refractive index of:

$$\frac{dn_e}{dT} = 2KP_s \frac{dP_s}{dT} \approx 7 \cdot 10^{-3} \frac{1}{{}^\circ C} \tag{61}$$

In the case of thin films, the polarization is constrained by substrate induced strain, resulting in a much lower value for dn_e/dT.

Since the ordinary index lies in a plane with no spontaneous polarization, the only effect on the index in that direction is from lattice thermal expansion. The concept of equation (53), that change in the index is proportional to strain, can be combined with the thermal expansion coefficient (α) to give:

$$\left(\frac{dn}{dT}\right)_{\exp ansion} = -\frac{\left(n^2-1\right)\left(n^2+2\right)}{6n^2}\alpha \approx -0.8\alpha \tag{62}$$

The expansion coefficients of BaTiO3 and of MgO around room temperature are on the order of 10^{-5} $°C^{-1}$. Equations (61) and (62) are opposite in sign, suggesting that for the extraordinary index there are competing effects in the change of index as a function of temperature.

Looking at Figure 45, the slope of n_{TE} is on the order of 10^{-5} $°C^{-1}$ and negative. This may indicate spontaneous polarization perpendicular to the film. It has been reported in the past that thermal stresses during post-growth cooling can induce such spontaneous poling [30]. This will also explain the positive slope seen in the pure $BaTiO_3$ as being due to the change in spontaneous polarization. The Hf doped $BaTiO_3$ is in the rhombohedral phase, as is evident both from the x-ray and from the discontinuities in the refractive index (n_{TM} in Figure 45). The changes in spontaneous polarization for rhombohedral $BaTiO_3$ are much smaller then those in the tetragonal phase, and therefore the slope of both n_{TE} and n_{TM} are only due to thermal expansion. This can also account for the small increase in n_{TM}

at 70°C, where the material goes through the phase transition into the tetragonal phase. Although this analysis is self-consistent, it lacks direct observation of the polarization. Further confirmation is required.

Chapter 6: Summary

1. Summary

The objectives of this research were to study the piezoelectric response of rhombohedral $BaTiO_3$ and the optical properties of $BaTiO_3$-based films.

The rhombohedral phase was successfully stabilized at room temperature by the addition of Zr, Hf, or KNb and the expected phase transitions were observed in the dielectric response. The enhanced electromechanical response was shown for all three systems, although the strain mechanism was not identical. Zr- and Hf- doped $BaTiO_3$ were piezoelectric, with a piezoelectric coefficient of d_{33}=290-470pc/N compared with d_{33}=75pC/N for pure $BaTiO_3$. KNb- doped $BaTiO_3$ was electrostrictive, with an electrostrictive coefficient of $Q_{33}=0.37m^4/C^2$, compared with $Q_{33}=0.11m^4/C^2$ for pure $BaTiO_3$. The maximum strain measured for the doped samples was 5-10 times higher then that of pure $BaTiO_3$.

The effect of growth conditions on the orientation and strain of $BaTiO_3$ thin films was studied. As the substrate temperature and laser fluency were increased the film orientation changed from (111) to (110), then to (100). Oxygen pressure had little effect on the orientation, although growth at pressures of less then 10^{-4}Torr O_2 resulted in the reduction of the $BaTiO_3$.

The growth of Zr- and Hf- doped $BaTiO_3$ on MgO has been demonstrated for the first time. The increase in lattice parameter due to doping resulted in a lower lattice mismatch with the substrate which in turn allowed deposition at lower temperatures. This is an important achievement for the introduction of $BaTiO_3$ to integrated optics. In addition, it has been demonstrated that the optical properties of the doped material are similar to those of pure $BaTiO_3$.

The index of refraction for the thin films was measured and a model based on the Clausius-Mossotti relation was used to explain the data. It was shown that variations in the index can be attributed to film orientation and strain. The refractive index for the $BaTiO_3$ films was extracted from the model, giving n_o=2.334 and n_e=2.163.

The growth of $BaTiO_3$ on SOI using an MgO buffer layer was demonstrated. Although the film quality was far from optimal, this preliminary result seems promising. More work is needed in order to optimize the growth conditions and improve film quality.

2. Conclusions

The feasibility of using rhombohedral $BaTiO_3$ as a piezoelectric actuator was demonstrated. In particular, $BaTiO_3$ doped with ~10%Hf showed comparable piezoelectric coefficient and strain levels to hard PZT (PZT8). Although the Curie temperature of PZT is higher then that of the $BaTiO_3$, many applications do not require operation at elevated temperatures, making Hf:$BaTiO_3$ attractive as a lead-free alternative.

The growth of Zr- and Hf- doped $BaTiO_3$ films on MgO was demonstrated to lower the processing temperature. This, in addition to the high electro-optic coefficient of $BaTiO_3$, makes them interesting candidates for integrated optics. $BaTiO_3$ is already used for its dielectric properties in ferroelectric memories. Furthermore, we have demonstrated that the piezoelectric properties of $BaTiO_3$ can be enhanced by the proper doping, making it a candidate for the actuator material in optical MEMS devices. Having one material system serve multiple purposes is very alluring, as it can simplify process flows and save time and money in fabrication.

Historically, $BaTiO_3$ has always been an important component in the field of ferroelectric materials and devices. This work showed that it has the potential to remain an important material in the future, extending the types of applications it can be used for.

3. Recommendations for Future Work

The focus of this work was to prove the feasibility of using the rhombohedral-stabilized $BaTiO_3$. Although this has been done, there are still some open questions that would require further research.

1. Electromechanical coupling coefficient – The electromechanical coupling is a very important parameter for actuator materials. Preliminary results suggest that the coupling coefficient for 10%Hf:$BaTiO_3$ is k^2~0.6 compared with k^2~0.4 for pure

$BaTiO_3$ and k^2~0.6-0.7 for PZT. This measurement, however, still needs to be verified, and other compositions need to be measured.

2. Single crystal growth – Some growth of single crystal Zr:$BaTiO_3$ was reported in recent years [22], although the single crystal properties reported are not much higher then the polycrystalline values reported in this work. More work is needed in order to understand whether that is due to intrinsic limitations or due to crystal quality in the reported work. In addition, other compositions should be examined, in particular the 10%Hf:$BaTiO_3$.

3. Optical loss measurements – Optical loss is a crucial parameter for optical devices. The optical loss in the films prepared in this work was too small to be measured by transmission perpendicular to the film. Work is now in progress to prepare waveguides that can be used to measure propagation loss.

4. Electro-optic coefficient – The electro-optic coefficient of the films has to be measured for it to be used in modulator structures. Some values have been reported for $BaTiO_3$ films on MgO [47], showing promising results. Further work is required, especially in determining the electro-optic coefficient of the doped $BaTiO_3$.

5. Film dielectric measurements – As mentioned earlier, the penetration of the electric field into the waveguide is crucial for the electro-optic effect. The RF dielectric constant of the $BaTiO_3$ films needs to be measured, and accounted for in the modulator design.

6. Integration on Si – Preliminary results showed that it is possible to integrate $BaTiO_3$ on Si by using thin MgO on SOI. The quality of these films still needs to be improved and the processing parameters need to be optimized.

Appendix A: Growth and Characterization of MgO

1. General

The growth of MgO films as a buffer layer was studied. This work is not directly related to the thesis, and therefore was not pursued to the fullest. It is for this reason that it is reported in an appendix.

2. Results and discussion

MgO was grown using PLD and sputtering. The sputtering allowed for a smoother, more uniform deposition. Figure 56 shows the thickness variations of MgO sputtered on Si. The variations are on the order of 0.1% over 2-3cm, compared with around 5-10% in the case of PLD (see for example Figure 37).

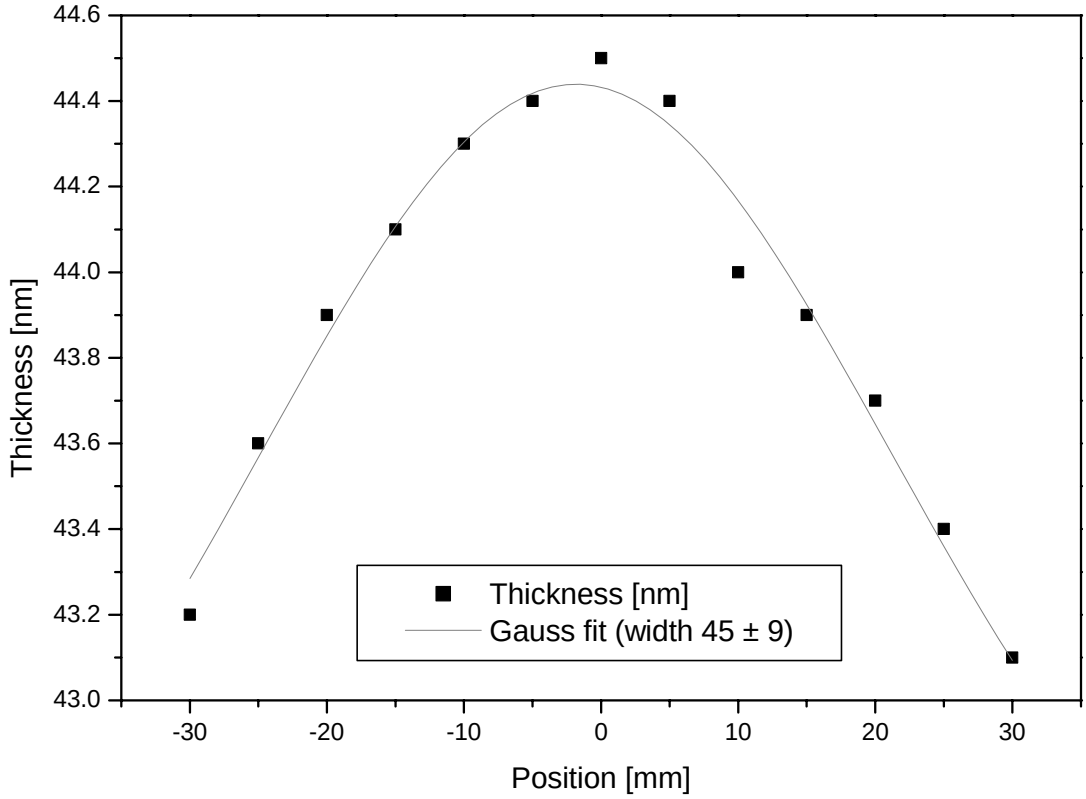

Figure 56: Thickness variations in sputter-deposited MgO

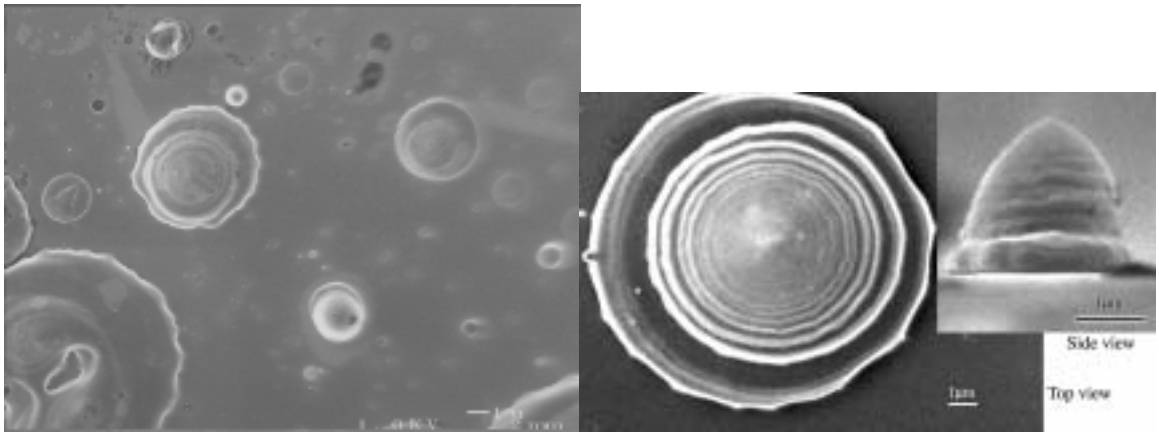

Figure 57: SEM image of MgO on Si showing droplets forming at high energy and low oxygen pressure.

Samples grown using PLD showed a large number of particulates on the surface. The particulates varied in size from 0.2-5μm, and were conical in shape. Using higher oxygen pressure and lower fluency resolved the problem. The appearance of particulates at high energy is common in PLD [44].

The advantage of the PLD was a higher deposition rate, important for creating a thick optical buffer for the $BaTiO_3$. In the case of growth on SOI, however, only a thin layer of MgO is needed. In this case, the higher film quality and thickness uniformity make sputtering a better suited technique. For future work on integrating $BaTiO_3$ on Si, it is planned to prepare the MgO on SOI using sputtering. Those samples will then be used as substrates for $BaTiO_3$ deposition.

References

[1] Goldschmidt, V.M., Shrifter Norske Videnskaps-akad, I: Mat. - Naturv. 2(1926).

[2] Von Hippel, A., Breckenridge, R.G., Chesley, F.G. and Tisza, L., Ind. Eng. Chem. 38, p. 1097-109(1946).

[3] Tuller, H.L. and Avrahami, Y. *Electroceramics*. in "Encyclopedia of Smart Materials"; edited by Schwartz, M.M. (John Wiley & Sons, New York, 2002) .

[4] Nye, J.F., Physical properties of crystals : their representation by tensors and matrices, (New York : Oxford University Press, 1985).

[5] Uchino, K., *Ferroelectric Devices*, (Marcel Dekker, New York, 2000).

[6] Ballantine, R.D.S., Martin, S.J., Ricco, A.J., Zellers, E.T., Frye, G.C. and Wohltjen, H., *Acoustic wave sensors : theory, design, and physico-chemical applications*, (Academic Press, San Diego, 1997)

[7] Swartz, S.L., "*Topics in electronic ceramics*", IEEE T Electr Insul 25 (5), *p.* 935-87(1990).

[8] Lee, S.G., Monteiro, R.G., Feigelson, R.S., Lee, H.S., Lee, M. and Park, S.E., "*Growth and electrostrictive properties of $Pb(Mg_{1/3}Nb_{2/3})O_3$ crystals*", Appl. Phys. Lett. 74 (7), *p.* 1030-2(1999).

[9] Uchino, K., *Piezoelectric actuators and Ultrasonic Motors*, (Kluwer Academic Publisher, Boston, 1997).

[10] Park, S.E. and Shrout, T.R., "*Ultrahigh strain and piezoelectric behavior in relaxor based ferroelectric single crystals*", J. Appl. Phys. 82 (4), p. 1804-11(1997).

[11] Hermans, C. and Tuller, H.L., "*Lead Hafnate Zirconate Titanate - based perovskite materials for actuation*", J. Eur. Ceram. Soc. 5 (1999).

[12] Park, S.E. and Shrout, T.R., "*Relaxor based ferroelectric single crystals for electro-mechanical actuators*", Piezoelectric Crystals Planning Workshop, 1997 .

[13] Chiang, Y.M., Farrey, G.W. and Soukhojak, A.N., "*Lead-free high strain single crystal piezoelectrics in the alkaline-bismuth-titanate perovskite family*", Appl. Phys. Lett. 73 (25), *p.* 3683-5(1998).

[14] Cross, L.E. *Ferroelectric ceramics: tailoring properties for specific applications*. in "Ferroelectric Ceramics: Tutorial Reviews, Theory, Processing, and Applications"; edited by Setter, N. and Colla, E.L. (Birkhaueser Verlag, Basel, Switzerland; Boston, MA, USA, 1993) p. 1-85.

[15] Jaffe, B., Cook, W.R. and Jaffe, H., *Piezoelectric ceramics*, (Academic Press, New York, 1971).

[16] Payne, W.H. and Tennery, V.J., "*Dielectric and structual investigations of the system $BaTiO_3$-$BaHfO_3$*", J. Am. Ceram. Soc. 48 (8), *p.* 413-7(1965).

[17] Verbitskaia, T.N., Zhdanov, G.S., Venevtsev, I.N. and Soloviev, S.P., "*Electrical and X-ray Diffraction Studies of the $BaTiO_3$ - $BaZrO_3$ System*", Soviet Phys. Cryst. 3, *p.* 182-92(1958).

[18] *Ferroelectric and Dielectric Thin Films*; Vol. 3, edited by Nalwa, H.S. , in Handbook of Thin Film Materials (Academic Press, London, 2002).

[19] Joshi, P.C. and Cole, M.W., "*Mg-doped $Ba_{0.6}$ $Sr_{0.4}$ TiO_3 thin films for tunable microwave applications*", Appl. Phys. Lett. 77 (2)(2000).

[20] Tura, V., Mitoseriu, L., Harnagea, C. and Ricinschi, D., "*Ferroelectricity in (Hf,Zr)-doped Barium Titanate Ceramics*", Ferroelectrics 239, *p.* 265-72(2000).

[21] Avrahami, Y. and Tuller, H., "*Rhombohedral-phase doped barium titanate as a piezoelectric transducer*", App. Num. US06744 200103, Pat. Pending, 2002 .

[22] Rehrig, P.W., ark, S.-E. , Trolier-McKinstry, S., Messing, G.L., ones, B. and hrout, T.R., "*Piezoelectric properties of zirconium-doped barium titanate single crystals grown by templated grain growth*", J. Appl. Phys. 86 (3), *p.* 1657-61(1999).

[23] Saleh, B.E.A. and Teich, a.C., *Fundamentals of photonics*, (Wiley, New York, 1991).

[24] Wessels, B.W., "*Ferroelectric oxide epitaxial thin films: synthesis and non-linear optical properties*", J. Cryst. Growth 195, *p.* 706-10(1998).

[25] Lee, M.-B. , Kawasaki, M., Yoshimoto, M. and Koinuma, H., "*Heteroepitaxial growth of $BaTiO_3$ films on Si by pulsed laser deposition*", Appl. Phys. Lett. 66 (11), *p.* 1331-3(1995)

[26] Tzing, W.H., Tuan, W.H. and in, H.L., "*The effect of microstructure on the electrical properties of NiO-doped $BaTiO_3$*", Ceramics International 25, *p.* 425-30(1999).

[27] Holman, R.L., Johnson, L.M.A. and Skinner, D.P., "*The desirability of electrooptic Ferroelectric Materials for Guided-Wave Optics*", 6th International Symposium on Applications of Ferroelectrics, Lehigh University, PA, USA, 1986 (IEEE), p. 32-41.

[28] Hoerman, B.H., Nichols, B.M., Nystrom, M.J. and Wessels, B.W., "*Dynamic response of the electro-optic effect in epitaxial $KNbO_3$*", Appl. Phys. Lett. 75 (18), *p.* 2707-9(1999).

[29] Jin, G.H., "*PLZT Film Waveguide Mach–Zehnder Electrooptic Modulator*", Journal of Lightwave Technology 18 (6), *p.* 807-12(2000).

[30] Srikant,V., Tarsa, E.J., Clarke, D.R. and Speck, J.S., "*Crystallographic orientation of epitaxial $BaTiO_3$ films: The role of thermal-expansion mismatch with the substrate*", J. Appl. Phys. 77 (4), *p.* 1517-22(1995).

[31] Baba, S., Mori, I. and Nakano, T., "*Precise determination of the refractive index of sputtered MgO thin films in the visible light range*", Vacuum 59, *p.* 531-7(2000).

[32] Eisenbeiser, K., Finder,J., Emrick, R., Rockwell, S., Holmes, J., Droopad, R., Yu, Z., Ramdani, J., Hilt, L., Talin, A., Edwards Jr., J., Ooms, W., Curless, J., Overgaard, C. and O'Steen, M., *RF Devices Implemented on GaAs on Si Substrates using a $SrTiO_3$ buffer layer*, (Motorola - Physical Science Research Labs, 2001).

[33] Speck, J.S. and Pompe, W., "*Domain configurations due to multiple misfit relaxation mechanisms in epitaxial ferroelectric thin films, 1. Theory*", J. Appl. Phys. 76 (1), *p.* 466-76(1994).

[34] Tuller, H. and vrahami, Y., "*Stabilized Barium Titanate Thin Film Structures*", App. Num. 60/405,297, Pat. Pending, 2002.

[35] Nunes, B.P., "*Edge-Defined Film-Fed Growth of Single-Crystal Piezoelectrics*", (Materials Science and Engineering, Massachusetts Institute of Technology, Cambridge, 2001) .

[36] Sayer, M., Judd, B.A., El-Assal, K. and Prasad, E., "*Poling of Piezoelectric Ceramics*", Journal of the Canadian Ceramic Society 50(1981).

[37] **Origin** ver. 6.0 (Microcal, Northampton, 1999).

[38] Jonker, G.H. and Kwestro, W., "*The trenary systems BaO-TiO_2-SnO and BaO-TiO_2-ZrO_2*", J. Am. Ceram. Soc. 41 (10), *p.* 390-4(1958).

[39] Haun, M.J., Furman, E., Jang, S.J. and Cross, L.E., "*Thermodynamic theory of the lead zirconate-titanate solid solution system, part I: phenomenology*", Ferroelectrics 99, *p.* 13-25(1989).

[40] Strukov, B. and Levanyuk,A.P., *Ferroelectric phenomena in crystals : physical foundations*, (Springer, New York, 1998).

[41] Jona, F. and Shirane, G., *Ferroelectric crystals*, (Macmillan Co., New York, 1962).

[42] Cullity, B.D., *Elements of x-ray diffraction*, 2d ed. (Addison-Wesley Pub. Co., Reading, Mass., 1978).

[43] Jackson, J.D., *Classical Electrodynamics*, 3rd ed. (John Wiley & Sons, New York, 1998).

[44] *Pulsed laser deposition of thin films*; edited by Chrisey, D.B. and Hubler, G.K. (John Wiley & Sons, New York, 1994).

[45] Gottmann, J. and Kreutz, E.W., "*Controlling crystal quality and orientation of pulsed-laser-deposited $BaTiO_3$ thin films by the kinetic energy of the film-forming particles*", Appl. Phys. A 70 (3), *p.* 275-81(2000).

[46] Ashcroft, N.W. and Mermin, N.D., *Solid state physics*, (Holt, Rinehart and Winston, New York, 1976).

[47] Beckers, L., Schubert, J., Zander, W., Ziesmann, J., Eckau, A., Leinenbach, P. and Buchal, C., "*Structural and optical characterization of epitaxial waveguiding $BaTiO_3$ thin films on MgO*", J. Appl. Phys. 83 (6), *p.* 3305-10(1998).